

## Synoptic fluctuation of the Taiwan Warm Current in winter on the East China Sea shelf

Jiliang Xuan<sup>1</sup>, Daji Huang<sup>1, 2</sup>, Thomas Pohlmann<sup>3</sup>, Jian Su<sup>3</sup>, Bernhard Mayer<sup>3</sup>, Ruibin Ding<sup>2, 1</sup>, Feng Zhou<sup>1, 2</sup>

<sup>1</sup>State Key Laboratory of Satellite Ocean Environment Dynamics, Second Institute of Oceanography,

5 State Oceanic Administration, Hangzhou, China

<sup>2</sup>Ocean College, Zhejiang University, Zhoushan, China

<sup>3</sup>Institute of Oceanography, University of Hamburg, Hamburg, Germany

*Correspondence to:* Daji Huang (djhuang@sio.org.cn)

### Highlights

- 10 ● Synoptic fluctuations of the wintertime Taiwan Warm Current appear mainly in two areas: north of  
Taiwan and the inshore area
- Synoptic fluctuation is mainly driven by the Taiwan Strait Current north of Taiwan and by wind in  
the inshore area
- Large Taiwan Strait Current intrusion generates a cross-shore transport from the coastal area to the  
15 offshore area
- Winter monsoon affects the alongshore transport of Taiwan Warm Current water between the 30  
and 100 m isobaths
- Winter monsoon affects the cross-shore transport of Taiwan Warm Current water at the latitudes  
20 26.5 °N and 28 °N

**Abstract.** The seasonal mean and synoptic fluctuation of the wintertime Taiwan Warm Current (TWC) were investigated using a well validated finite volume community ocean model. The spatial distribution and dynamics of the synoptic fluctuation were highlighted. The seasonal mean of the wintertime TWC has two branches: an inshore branch between the 30 and 100 m isobaths and an offshore branch between the 100 and 200 m isobaths. The Coriolis term is much larger than the inertia term and is almost balanced by the pressure gradient term in both branches, indicating the geostrophic balance of the mean current. Two areas with significant fluctuations of the TWC were identified during wintertime. One of the areas is located to the north of Taiwan with velocities varying in the cross-shore direction. These significant cross-shore fluctuations are driven by barotropic pressure gradients associated with the intrusion of the Taiwan Strait Current (TSC). When a strong TSC intrudes to north of Taiwan, the isobaric slope tilts downward from south to north, leading to a cross-shore current from the coastal area to the offshore area. When the TSC intrusion is weak, the cross-shore current to the north of Taiwan is directed from offshore to inshore. The other area of significant fluctuation is located in the inshore area, extending in the region between the 30 and 100 m isobaths. The fluctuations are generally strong in the alongshore direction, in particular at the latitudes  $26.5^{\circ}\text{N}$  and  $28^{\circ}\text{N}$  where they are important for the local cross-shore transports. Wind affects the synoptic fluctuation through episodic events. When the northeasterly monsoon prevails, the southward Zhe-Min Coastal Current dominates the inshore area associated with a deepening of the mixed layer. When the winter monsoon is weakened or the southerly wind prevails, the northward TWC dominates in the inshore area.

40

**Keywords:**

Synoptic fluctuation, East China Sea, Taiwan Warm Current, Taiwan Strait Current, Kuroshio

## 1 Introduction

45

On the East China Sea (ECS) shelf, the mean path of the Taiwan Warm Current (TWC) has two branches: the inshore branch along the 50 m isobath and the offshore branch along the 100 m isobath (Su and Pan, 1987). The summer TWC has been well studied because the current is stationary and strong, with an average speed of 0.3 m/s (Guan, 1978; Fang et al., 1991; Isobe, 2008; Yang et al., 2011, 2012). The spatial structure and temporal variation of the wintertime (December to March) TWC are less known due to its surface weak mean velocity, according to a climatological structure of the surface current in the ECS mapped by Qiu and Imasato (1990).

50

The wintertime TWC on the ECS shelf shows synoptic fluctuations (Cui et al., 2004; Zhu et al., 2004; Zeng et al., 2012; Huang et al., 2016). These synoptic fluctuations show some features common with those over other continental shelves, i.e., they have periods between 3 and 15 days and are associated with coastal sea level changes, which can be explained by local winds or by coastal trapped waves (Huyer, 1990; Brink, 1991; Huthnance et al., 1986). Huang et al. (2016) have shown that the wind was a main physical factor which caused the temporal variation of the wintertime currents at the synoptic scale in the coastal area of the ECS. However, the dominant physical factors of the TWC fluctuations are still lack of study, regarding that the fluctuations on the whole shelf of the ECS may be more complicated due to the complex bottom topography, alternating monsoon forcing and conjunction of several current systems such as the Kuroshio Current, the Taiwan Strait Current (TSC) and the Zhe-Min Coastal Current (ZMCC). These synoptic fluctuations are also known to influence the regional material transport,

60

65 especially when the amplitude of the fluctuations is comparable to, or even larger than, the mean current. On the ECS shelf, some recent observations have shown that the TWC has an episodic wintertime feature (Zhu et al., 2004) and the intermittency of the TWC in winter has an amplitude as large as 0.2 m/s (Zeng et al., 2012). Moreover, it has been observed that the intermittency of the TWC in winter causes a cross-shore current which is closely linked to the alongshore component (Huang et al., 2016). Therefore, we focus on studying the spatial patterns of synoptic fluctuations to better understand the role of the wintertime TWC on the cross-shore water exchange.

A comparison between the wintertime climatological density (Fig. 1a) and synoptic density distributions observed during two surveys (Figs. 1b and 1c) suggests that two distinct areas with significant synoptic fluctuations exist. The climatological density is taken from the Generalized Digital Environment Model (GDEM, Carnes, 2009) data, and the two surveys were carried out in February 2007 by two research vessels. Because the isopycnal lines are closely related to geostrophic currents, we can infer the strength of the TWC from the horizontal gradient of the isopycnals between  $24\text{-}\sigma_t$  and  $25\text{-}\sigma_t$  contours (Fig. 1a). This accounts for the fact that in winter the water mass of TWC is located in this density range [according to the hydrography analysis of Su et al. (1994)]. The two-branch structure of the TWC can be inferred from the wintertime climatological density. In this paper, we defined that the near-coast area is the area between the coast and 30 m isobath where the ZMCC occurs; the inshore area is the area between the 30 and 100 m isobaths where the TWC inshore branch dominates; and the offshore area is the region between the 100 and 200 m isobaths where the TWC offshore branch prevails. According to the hydrographic data analysis and numerical interpretation by Su and Pan (1987), the TWC inshore and offshore branches mainly occur in those specific isobaths. However, these two branches were missing during the two

synoptic surveys (Figs. 1b and 1c), indicating strong synoptic fluctuations of the TWC on the ECS shelf.

Furthermore, the density anomalies between the two surveys and the GDEM data (Figs. 1d and 1e)

indicate that the most significant fluctuations are located north of Taiwan and in the inshore area. Both

90 surveys show negative density anomalies north of Taiwan, indicating that the TWC was weak and that

less low-density coastal water was transported to the ECS shelf during the observational periods. The

density anomalies in the inshore area show different patterns for the two synoptic surveys, with a positive

anomaly in the first survey (Fig. 1d) and a negative anomaly in the second (Fig. 1e), indicating a much

stronger synoptic fluctuation in the inshore area.

95

Figure 1

Candidate factors for driving these synoptic fluctuations are local wind, surface cooling, and the upstream

currents of the Kuroshio Current and the TSC. As discussed by Huyer (1990), wind is often considered

100 as the major driving mechanism of synoptic fluctuations of the wintertime TWC. The northeasterly

monsoon wind in winter blows against the northeastward TWC and produces a southwestward ZMCC

(Chuang and Liang, 1994; Oey et al., 2010). Zhu et al. (2004) suggested that the occurrence and duration

of the TWC are associated with the meandering of the Kuroshio Current north of Taiwan. The

northeastward TSC, as an upstream flow of the TWC, also influences the synoptic fluctuation of the

105 wintertime TWC. Hong et al. (2011) and Hu et al. (2010) summarized that the temporal and spatial

variation of TSC is modulated by strong monsoon forcing, complex topography and circulation in the

northern South China Sea as well as coastal water input and the Kuroshio intrusion. Guan and Fang

(2006) showed evidence that the TSC and the TWC merge in the area between the Taiwan Strait and the

Zhe-Min coastal region. Takahashi and Morimoto (2013) pointed out that the temporal variation of the  
110 TWC is characterized by the propagation of vorticity anomalies originating from northeast of the Taiwan  
Strait, which further demonstrated that the fluctuations of TWC was associated with its upstream currents  
such as the TSC.

To explore the spatial distribution of synoptic fluctuations of the wintertime TWC on the ECS shelf,  
115 current data with high resolution in both space and time are required. Previous studies on the wintertime  
TWC were based on cruise surveys (Su and Pan, 1987; Chen et al., 1994; Chen and Wang, 1999),  
anchored mooring observations (Zhu et al., 2004; Zeng et al., 2012; Huang et al., 2016) and numerical  
simulations (Guo et al., 2003, 2006; Yang et al., 2011, 2012; Xuan et al., 2012, 2016). The observation  
data are limited in terms of temporal and spatial coverage; hence, they cannot fully reveal the synoptic  
120 fluctuations of the TWC and their regional differences. Numerical simulations provide a promising  
approach for studying the overall structure and driving mechanisms of synoptic fluctuations of the TWC  
in more detail.

In this study, the Finite Volume Coastal Ocean Model (FVCOM; Chen et al., 2003) is used to investigate  
125 synoptic fluctuations and their mechanisms of the wintertime TWC. The rest of this paper is organized  
as follows. In Sect. 2, we provide a description of methods and validation. The mean distribution,  
synoptic fluctuations, and dynamic diagnostics of the wintertime TWC are given in Sect. 3. The impact  
of synoptic fluctuation on water exchange is further discussed in Sect. 4, followed by conclusions in Sect.  
5.

130

## 2 Methods and validation

### 2.1 Model configuration

To investigate the currents (TWC, Kuroshio Current, ZMCC, etc.) and their synoptic fluctuations on the ECS shelf, a 3-D unstructured-grid (Fig. 2, left panel) FVCOM is developed for the entire Bohai, Yellow, and East China Seas (part of the Japan/East Sea, and part of the Pacific Ocean). A regional refinement of the resolution (approximately 3 km) is specified around the ECS shelf break at the 200 m isobaths, where a strong excursion of the Kuroshio Current also occurs. The General Bathymetric Chart of the Oceans (GEBCO) provides high-resolution (approximately 1 km) bathymetric data (Smith and Sandwell, 1997). Twenty vertical layers with 76954 triangle cells were specified in the water column in a sigma-stretched coordinate system.

The driving forces of the numerical simulation include tides, river discharge, surface heat fluxes, wind, and open boundary conditions. Harmonic constants of 11 major tidal constituents ( $M_2$ ,  $S_2$ ,  $N_2$ ,  $K_2$ ,  $K_1$ ,  $O_1$ ,  $P_1$ ,  $Q_1$ ,  $M_4$ ,  $MS_4$ , and  $MN_4$ ) were used; these are based on the Oregon State University global inverse tidal model TPXO.7.0 (Egbert et al., 1994; Egbert and Erofeeva, 2002). The daily-mean river discharge of the Changjiang and Huanghe were taken from publicly available observation data at the Datong hydrometric station (<http://yu-zhu.vicp.net/>). Other rivers were not included because of their small discharges, e.g., the Qiantang River, with the largest runoff from the Zhejiang coast, has a climatological mean discharge in winter of about  $230 \text{ m}^3/\text{s}$ , which is nearly negligible compared to the Changjiang winter discharge of about  $11500 \text{ m}^3/\text{s}$ . The daily-mean heat fluxes were from the objectively analyzed air-sea fluxes (Yu and Weller, 2007), and the 3-hourly wind stress and 10 m wind speed data was from the ERA-40 re-analysis (Uppala et al., 2005). The open boundary conditions, including daily temperature,

salinity, and fluxes at the Taiwan Strait, the western Pacific Ocean, and the Japan/East Sea, were obtained from the Hybrid Coordinate Ocean Model (Bleck, 2002) and interpolated onto the FVCOM model grid points. The temporal resolution of all the driving force fields is better than or equal to one day, which is essential to resolve synoptic fluctuations.

The hindcast outputs of sea surface height, temperature, salinity, and velocities for the five years of simulation from 2009 to 2013 are used, following three spin-up years (2006-2008) initiated with the temperature and salinity taken from the Hybrid Coordinate Ocean Model and velocity set to zero. The initial conditions are ramped-up over a period of 30 days and that at the lateral boundaries sponge layer was used with the same method as Chen et al. (2008). The model time step was 15 seconds for the 2-D barotropic mode and 90 seconds for the 3-D baroclinic mode. All of the output fields were processed with a tidal filter (Godin, 1972) to remove tidal oscillations (considering that the major time scale of synoptic fluctuations in this study area is 3–15 days).

Since the currents in 2009 could partly be validated by means of available observational data (see Sect. 2.2), the currents from January 1 to February 28, 2009 were selected for analysis of the wintertime TWC.

## 2.2 Validation of the mean currents and synoptic fluctuations

The mean currents, e.g., the Kuroshio Current, the TWC, and the ZMCC, were calculated by averaging the outputs of January and February 2009. We validated the mean currents in terms of circulation structure, boundary fluxes, and coastal currents.



175 The FVCOM has reproduced almost all of the known circulation structure in the ECS in winter. The surface mean currents (Fig. 2) shows three major currents: the Kuroshio Current, the TWC, and the ZMCC. The Kuroshio Current, with a speed of about 1 m/s, enters the ECS just northeast of Taiwan and flows along the shelf break up to the northern area and ultimately leaves the ECS through the Tokara Strait. Both the route and strength of the Kuroshio are comparable with those reported in the literature  
180 (Guan, 1978; Qiu and Imasato, 1990). The TWC has two northward branches, one inshore (between the 30 and 100 m isobaths) and another offshore (between the 100 and 200 m isobaths), which is consistent with Su and Pan (1987). The southward directed ZMCC in the nearshore area from the Changjiang Estuary to the Taiwan Strait agrees well with that reported in previous studies (Guan and Mao, 1982; Zeng et al., 2012).

185

The simulated volume transports across the Taiwan Strait, the East Taiwan Channel, the Tsushima Strait, the Tokara Strait, and the shelf break of the 200 m isobath were validated using results from the literature (Table 1). The simulated transports were accurate enough to reproduce volume transport (1.22 Sv) through the Taiwan Strait which is closer to the observation value (1.20 Sv) from Isobe (2008) than  
190 former model results. The volume transports across the Taiwan Strait and the Tokara Strait, and the cross-shore exchange, affected the path and magnitude of the TWC. The annual mean transport across the 200 m isobath toward the shelf is 1.66 Sv, which is balanced by the inflow from the Taiwan Strait (1.22 Sv) and the outflow through the Tsushima Strait (2.85 Sv).

195

Figure 2

Table 1

Figure 3 shows a comparison between simulation and observation results for the alongshore currents and  
200 the cross-shore currents on the ECS shelf. The observational data were obtained from four mooring  
surveys (Fig. 2, red stations) off the Zhe-Min coast (Zeng et al., 2012). The observed and simulated  
currents were both averaged for the observational period, which was from January 1 to February 28,  
2009. Using the same method as in Huang et al. (2016), we defined the positive alongshore current  
directing from southwest ( $218^\circ$ ) to northeast ( $38^\circ$ ), which is the mean tangential direction of the isobaths  
205 on the southwestern shelf of the ECS. The positive cross-shore direction is the mean normal direction of  
the isobaths from northwest ( $308^\circ$ ) to southeast ( $128^\circ$ ). The alongshore components (Figs. 3a and 3b)  
show that the ZMCC flows southwestward parallel to the coast in winter, with a maximum speed of 0.15  
m/s along the 30 m isobath. The TWC flows northeastward with a speed of 0.05 m/s, and the core is  
located in the lower layer at about 50 m at Station 4. The cross-shore component (Figs. 3c and 3d) is  
210 much weaker than the alongshore components, and it shows a complex spatial pattern. It flows offshore  
in the upper layer and onshore in the lower layer at Station 1. Moreover, it mainly flows onshore at  
Station 2, and it flows offshore in the entire water column at Stations 3 and 4. Altogether, the simulated  
pattern and magnitude both of the alongshore and cross-shore components are in good agreement with  
the observations. However, there are some differences between the observed and simulated results; for  
215 example, the simulated ZMCC occupies a broader space than that in the observations. This may have  
been caused by the relatively low number of observational stations.

Figure 3

220 Synoptic fluctuations of the TWC inshore branch during January and February 2009 were also validated against the mooring results (Fig. 4). Since the TWC shows a strong signature at Station 4, the time series of the alongshore currents and cross-shore currents in the whole water column of Station 4 were used for the validation. To eliminate the influence of local effects, the simulated currents were averaged in a  $10 \times 10 \text{ km}^2$  area around Station 4. Both the observed and simulated results show that the TWC fluctuates with a period of 3–15 days. The simulated TWC (Fig. 4a, warm color) appeared stronger ( $> 0.1 \text{ m/s}$ ) on Jan. 7, Jan. 12, Jan. 18, Jan. 21, Jan. 26, Jan. 29, Feb. 10, Feb. 14, Feb. 19, Feb. 22, and Feb. 25, which agrees well with data from the observations (Fig. 4b). The time series of the simulated cross-shore component (Fig. 4c) are virtually in phase with the observations (Fig. 4d). In contrast to the anisotropic feature for the mean currents (Fig. 3), i.e., that the alongshore component is nearly one order of magnitude larger than the cross-shore component in the mean condition, the magnitude of the cross-shore fluctuations is comparable to the alongshore fluctuations.

Figure 4

### 235 **2.3 EOF analysis of synoptic fluctuations**

The Empirical Orthogonal Function (EOF) method (Emery and Thomson, 2001), as a statistical method, has been used to understand synoptic fluctuations of the wintertime TWC. The simulated currents from Jan. 1 to Feb. 28, 2009 were selected and their anomalies were calculated. Then, using the Matlab EOF-function, the current vectors were separated into several orthogonal modes to show the spatial and temporal variations. Because the first two leading modes explain 91 % of the total variance, only these

two modes were used for the analysis.

The spatial distributions of the two leading EOF modes were used to analyze the regional difference of the synoptic fluctuations. To investigate the driving force of the two EOF modes, the temporal variation  
245 was compared to the potential influence factors, such as wind, upstream currents, and net surface heat flux.

## 2.4 Momentum analysis

The driving mechanisms of the synoptic fluctuations were further analyzed using the momentum  
250 equation. First, the momentum balance as implemented in FVCOM (Chen et al., 2003) is shown in Eq. (1). The three terms on the left hand side represent local acceleration, Coriolis acceleration, and advection, respectively, and the three terms on the right hand side represent pressure gradient, friction, and diffusion, respectively.

$$\frac{\partial \bar{V}}{\partial t} - 2\bar{\Omega} \times \bar{V} + (\bar{V} \cdot \nabla) \bar{V} = -\frac{1}{\rho_0} \nabla P + \frac{\partial}{\partial z} (K_m \frac{\partial \bar{V}}{\partial z}) + \bar{F}, \quad (1)$$

255 where  $\bar{V}$  is velocity,  $\bar{\Omega}$  is the Earth's rotation angular velocity,  $\rho_0$  is the average density,  $P$  is pressure,  $K_m$  is the vertical eddy viscosity coefficient, and  $\bar{F}$  is horizontal diffusion.

Second, according to the hydrostatic approximation used in FVCOM [as shown in Eq. (2)], the pressure gradient is given as the product of density times the gravitational acceleration. This results in Eq. (3),  
260 which indicates that pressure gradient can be decomposed into the effects of the barotropic and baroclinic components, as shown in Eq. (4).

$$\frac{\partial P}{\partial z} = \rho g, \quad (2)$$

$$P_z = \int_z^\eta \rho g dz = \int_z^\eta (\rho_0 + \rho') g dz = \rho_0 g(z + \eta) + \int_z^\eta \rho' g dz, \quad (3)$$

$$\nabla \bar{P} = \rho_0 g \nabla \eta + \nabla \left( \int_z^\eta \rho' g dz \right), \quad (4)$$

265 where  $\rho$  is density,  $\rho'$  is density anomaly,  $g$  is the gravitational acceleration, and  $\eta$  is sea surface height.

Finally, the momentum equation is vertically integrated to estimate momentum balance for the water column. Since the horizontal diffusion is a comparably small term, it is neglected for simplicity.

$$270 \quad \int_{-H}^0 \frac{\partial \bar{V}}{\partial t} + \underbrace{\int_{-H}^0 -2\bar{\Omega} \times \bar{V}}_{\text{Coriolis}} + \underbrace{\int_{-H}^0 (\bar{V} \cdot \nabla \bar{V})}_{\text{Advection}} = \underbrace{-gH \nabla \eta}_{\text{Barotropic}} - \underbrace{\int_{-H}^0 \nabla \left( \int_z^\eta \rho' g dz \right)}_{\text{Baroclinic}} + \underbrace{\rho_a C_D |\bar{U}| \bar{U}}_{\tau_a} - \underbrace{k_b |\bar{U}_b| \bar{U}_b}_{\tau_b}, \quad (5)$$

*Total Pressure*

where  $\tau_a$  is wind stress and  $\tau_b$  is bottom stress,  $\rho_a$  is the density of air,  $\bar{U}$  is the wind speed at 10 m above sea surface,  $C_D$  is a drag coefficient at the sea surface (which varies with wind speed  $\bar{U}$ ),  $k_b$  is a bottom friction coefficient ( $k_b = 0.005$ ), and  $\bar{U}_b$  is the simulated velocity at the bottom.

275

### 3 Results

#### 3.1 Mean distribution of TWC in winter

Since the observational results (Su and Pan, 1987; Zeng et al., 2012) show that both branches of the wintertime TWC are flowing in the subsurface, we use the vertical maximum velocity (VMV) and its  
280 corresponding depth as two indices to quantify the strength of the subsurface currents (Fig. 5).

As stated above, the distribution of the VMV shows two branches of the TWC (Fig. 5a). The inshore branch (Fig. 5a, blue arrow of IB), which was located between the 30 and 100 m isobaths, followed a straight route from the northwest of Taiwan to the northern ECS shelf. The offshore branch (Fig. 5a, blue arrow of OB) existed near the 100 m isobath and had a horizontal structure with two meanders. The two meanders turn to the cross-shore direction along latitudes 26.5°N and 28°N. These two branches are further illustrated in the distributions of current speed along the six cross-TWC sections (S1-S6), which were located at critical points in the two meanders (Fig. 6). From the VMV structure, it can be inferred that the intrusions of the TSC and the Kuroshio Current both affected the origin of the offshore branch (Fig. 6, S1-S3).

We further examined the subsurface current core using the depth of the VMV (Fig. 5b). We found that the VMV of the TWC was located 40–60 m below the surface at the inshore branch and 20–40 m below the surface at the offshore branch. Figure 6 shows the VMV positions in the subsurface layer; it also illustrates that the depth of the subsurface VMV in the inshore branch was deeper than that in the offshore branch. The northerly wind in winter weakens the northward TWC, particularly in the upper layer, which leads to the formation of the subsurface VMV. Assuming a relatively spatially homogeneous heat loss, a different cooling occurs, due to the smaller heat capacity of the shallow coastal water compared to the deeper offshore waters; hence generating a horizontal density gradient leading to a southeastward vertical current shear according to the thermal wind relationship, resulting in an increasing southwestward flow component from surface to bottom, which in turn weakens the northeastward flow of the TWC inshore branch. Therefore, the fact that the depth of the subsurface current core in the inshore branch is greater than that in the offshore branch indicates that the effects of baroclinicity and wind friction on the inshore

branch are stronger than the offshore branch.

305

The magnitude of the wintertime TWC was obtained by flux analysis. Two dividing lines (Fig. 5a, red lines) were defined as the boundaries for the ZMCC, the TWC inshore branch, and the TWC offshore branch, which had the weakest flows. The flux of each branch (Fig. 5c) was calculated using the horizontal integration between the boundaries and the vertical integration in the water column. The inshore branch intensifies along its way and becomes significant north of 26.5 °N, showing particularly strong flow velocities between 27.5 and 28.0 °N. In this area, the subsurface current was much stronger from S4 to S5 than in the other areas (Fig. 6). The flux in the entire offshore branch was large, particularly north of Taiwan.

315

Figure 5

Figure 6

### 3.2 Synoptic fluctuations

320

The observations (Fig. 4) have demonstrated that the synoptic fluctuation in the TWC inshore branch (near 121.5 °E, 27.0 °N) is significant. We further investigated the regional difference of fluctuations in the two TWC branches in winter 2009 using the following three steps: (i) two regions with significant fluctuations are identified by the current standard deviations of the VMV (Fig. 7) and the corresponding temporal variation of vertical structures at their extremes (Fig. 8); (ii) each of the two significant fluctuations is decomposed into EOF components (Fig. 9), and (iii) the influence factors, such as wind,

325

upstream currents, and net surface heat flux, are investigated by examining their correlations with the first two leading EOF components (Figs. 10 and 11).

The current standard deviations (Fig. 7) shows that prominent fluctuations occurred in two regions: north of Taiwan and the inshore area. The standard deviations of VMV at the two regions were larger than 0.1 m/s (comparable to the mean currents). In the area north of Taiwan, the fluctuation was located in the origin area of the TWC offshore branch. The fluctuation in this region was in phase with the fluctuation in the Taiwan Strait, indicating that the TSC played an important role in generating the fluctuation north of Taiwan (to a greater extent than did the Kuroshio intrusion). The TWC fluctuation had a strong magnitude in the cross-shore direction, which means the fluctuation transported the water north of Taiwan to both the inshore and offshore branches. In the inshore area, the fluctuation was located in a wide region between the 30 and 100 m isobaths, where the southwestward flowing ZMCC and the northeastward directed TWC meet. As deduced from the standard deviation, the currents fluctuated significantly in the alongshore direction, indicating that the TWC inshore branch occurred episodically.

340

Figure 7

The vertical structures of the fluctuations north of Taiwan and in the inshore area at two representative points and their relation with upper mixed layer depth are further analyzed (Fig. 8). The major component (the alongshore current) of the TWC in each of the two regions (P1 and P2, Fig. 7) is used to show the vertical structure of the fluctuation. The depths of the upper mixed layer were determined by a Richardson number criterion (Mellor and Durbin, 1975; Grachev et al., 2013; Richardson et al., 2013),



where the critical Richardson number equals 0.25 in this paper [as in Xuan et al. (2012)]. The mean depth of the upper mixed layer north of Taiwan (20 m) was much shallower than the mean depth in the inshore area (42 m). However, the TWC (Fig. 8, warm color) fluctuated with significant variations of the upper mixed layer depth (Fig. 8, gray lines) in both areas. When the upper mixed layer deepened, the northeastward TWC (Fig. 8, warm color) was weakened or even replaced by the southwestward ZMCC, and vice versa. Hence, wind and surface cooling, which both drive the mixed layer depth, can affect the TWC fluctuation.

355

Figure 8

The TWC fluctuations were further decomposed into EOF modes. The first two leading EOF modes account 54% and 37% of the total variances (Fig. 9), which were associated with the two prominent fluctuations north of Taiwan and in the inshore area (Fig. 7). Both EOF modes had a maximum fluctuation larger than 0.2 m/s (comparable to the mean currents). The spatial pattern of the first EOF mode (EOF1, Fig. 9a) shows that the fluctuation continued from the Taiwan Strait to the area north of Taiwan, indicating that the fluctuation north of Taiwan was related to the TSC and not to the Kuroshio Current. The alongshore component also showed a strong fluctuation in the Taiwan Strait, which means that the TSC episodically intruded the shelf. The cross-shore component revealed a great fluctuation north of Taiwan that was larger than 0.1 m/s. This cross-shore fluctuation impacted on the trajectory of the TWS water, synoptically flowing into the TWC inshore branch, offshore branch, or Kuroshio Current.

The spatial pattern of the second EOF mode (EOF2, Fig. 9b) shows a synoptic fluctuation in the inshore

370 area. The fluctuation mainly varied in the alongshore direction, which indicates the episodic occurrence  
of the TWC inshore branch. The area with alongshore fluctuation (Fig. 9d) larger than 0.1 m/s was located  
between the 30 and 100 m isobaths, which demonstrates that the TWC could also episodically affect this  
area. In addition, there were cross-shore fluctuations in the inshore area (Fig. 9f), mostly along the  
latitudes 26.5°N and 28°N. The latitudes of great cross-shore fluctuations agreed well with the latitudes  
375 where the TWC offshore branch of the mean currents (Fig. 5a) turned to the cross-shore direction. This  
indicated that the cross-shore transports were most significant at the latitudes 26.5°N and 28°N,  
according to both the mean currents and the synoptic fluctuations.

Figure 10 shows the temporal variation of EOF1 and its relation with north-south component of wind  
380 speed, net surface heat flux, the TSC, and the Kuroshio Current. We found a close correlation between  
EOF1 and TSC ( $R = 0.86$ ), demonstrating that the TSC played the most important role in generating the  
TWC fluctuation north of Taiwan. The EOF1 and TSC were positively correlated, meaning that a larger  
TSC intrusion north of Taiwan leads to a cross-shore current from the coastal area to the offshore area  
and that a weak TSC intrusion causes a cross-shore current from offshore to inshore north of Taiwan.

385

Figure 11 shows the temporal variation of EOF2 and its relation with the north-south component of wind  
speed, net surface heat flux, the TSC, and the Kuroshio Current. It can be seen that EOF2 and wind are  
well correlated ( $R = 0.89$ ), indicating the important role of wind in generating the TWC fluctuation in  
the inshore area. The northerly monsoon would greatly enhance the southwestward ZMCC, which  
390 replaces the northeastward TWC in the inshore area. Together with the effect of net surface heat flux, the  
stronger northerly monsoon during Jan. 5-13, Jan. 19-25 and Feb. 16-18 causes the deepening of the

mixed layer (P2, Fig. 8).

Figure 9

395

Figure 10

Figure 11

### 400 3.3 Dynamic diagnostics

The wintertime (January and February 2009) mean of the water column momentum balance (Fig. 12) is used to show the overall distribution of the fundamental forces over the ECS shelf. The Coriolis force (Fig. 12a) is mainly balanced by the total pressure (Fig. 12b) in both branches, indicating the dominant role of geostrophic balance in the wintertime TWC. However, the wind-induced surface friction plays an important role in the TWC, especially in the inshore area and the Taiwan Strait (Fig. 12c). The bottom friction has an impact north of Taiwan and in the shallow Taiwan Strait, in particular when significant Kuroshio intrusion enhances the bottom flow (Fig. 12d). The effects of advection and acceleration are predominantly local indicated by mostly incoherent small scale distributions (Figs. 12e, 12f), so they can be ignored when studying the large-scale current of the wintertime TWC.

410

Figure 12

The variation of the driving forces at two representative points P1 and P2 were used to analyze the dynamics of synoptic fluctuations north of Taiwan and in the inshore area. Regarding the results from the EOF analysis, the three force terms, namely Coriolis, total pressure, and wind (Fig. 13), were selected to investigate the effect of the TSC on the fluctuation north of Taiwan (Fig. 9a) and the effect of wind on the fluctuation in the inshore area (Fig. 9b).

In the area north of Taiwan, the cross-shore fluctuations were induced by the TSC intrusion. The variation of alongshore Coriolis force (Fig. 13a, black line) was much greater than the cross-shore Coriolis force (Fig. 13b, black line), which means that the fluctuation north of Taiwan was mainly in the cross-shore direction. The Coriolis force (Fig. 13a, black line) was mainly balanced by the total pressure (Fig. 13a, blue line), which means the currents fluctuations north of Taiwan are dominated by geostrophic balance. As mentioned in Sect. 3.2, the TWC fluctuation north of Taiwan was associated with the TSC rather than with the Kuroshio Current. Therefore, in the shallow coastal area the TSC mainly caused variations in the depth-independent barotropic pressure gradients, which further generated the cross-shore fluctuation. The mechanism can be interpreted as follows. When a larger TSC intrusion occurred, the isobaric slope tilted downward from south to north, generating a cross-shore current from the coastal area to the offshore area. On the contrary, when the TSC intrusion was weak, the Kuroshio intrusion from offshore to inshore dominated north of Taiwan.

Wind friction (Figs. 13c and 13d) was a fundamental factor in generating the fluctuations in the inshore area. Although the geostrophic balance dominated in the inshore branch for most of the time, the episodically strong winter monsoon had an important role in generating the TWC fluctuations. The

435 northwestward direction Coriolis force (Fig. 13c, black line) shows that the southwestward ZMCC occurred on Jan. 12, Jan. 22, and Feb. 14, 2009 and was associated with a northerly wind (Fig. 13c, red line). It indicates that strong northerly monsoon in winter can reduce or even stop the northeastward TWC in the inshore area, causing the intermittency of the TWC inshore branch.

440

Figure 13

#### 4 Discussion

The simulated results in the winters of the years 2010 to 2013 (Fig. 14) show that general structures of the TWC in the other winters were similar to that in winter 2009 (Fig. 5 and Fig. 9), which indicates that 445 the results from the winter 2009 can be regarded as representative for the winter situation. The two TWC branches and the two areas of strong fluctuations were presented in the all winters from of 2009 to 2013, although their strength showed a certain inter- annual variability in accordance with the changing surface forcing and boundary fluxes.

450

Figure 14

The wintertime TWC, which is manifested by with two subsurface branches and significant synoptic fluctuations, has a very different structure when compared with the stationary and surface summertime TWC reported in previous studies (Guan, 1978; Fang et al., 1991; Isobe, 2008). The synoptic events, 455 with time scales of 3-15 days, play a dominant role on the horizontal advective transports. According to Ledwell et al. (1998) synoptic variations are much more effective on the horizontal transport than

variations on shorter time scales. The synoptic fluctuations modulate the spatial structure of the wintertime TWC, especially when their magnitudes are comparable with that of the mean currents, such as the two prominent fluctuations north of Taiwan and in the inshore area (Fig. 7). Therefore, the two prominent fluctuations will be discussed next in terms of their contributions to the alongshore and cross-shore transports.

#### **4.1 Cross-shore transport north of Taiwan induced by the TSC**

In the area north of Taiwan, the TSC intrusion generated strong fluctuations of the TWC in the cross-shore direction (Fig. 9a). When a larger TSC intrusion occurred, the isobaric slope tilted downward from south to north, generating a cross-shore current from the coastal area to the offshore area. Compared to the reported summer route that transports Taiwan Strait water to the inshore area between the 30 and 100 m isobaths (Guan, 1978; Fang et al., 1991; Isobe, 2008; Yang et al., 2011, 2012), our results showed that most Taiwan Strait water was transported to the TWC offshore branch and to the Kuroshio area as a result of the cross-shore fluctuations induced by the synoptic TSC intrusion.

A numerical tracer simulation was used to analyze the role of the cross-shore fluctuation in the transport of the TSC water and the Kuroshio water north of Taiwan. In order to demonstrate the characteristics of the flow patterns more clearly, artificial tracers are released in the model domain and transported by the velocity field provided by the FVCOM simulation. The tracer running was part of the FVCOM simulation; therefore, all the above mentioned dynamics were involved, e.g., tide, wind, and boundary forces. The release location and start date of the particles were configured as follows. Two sections, one in the Taiwan Strait (Fig. 15a, black dots) and another in the East Taiwan Channel (Fig. 15b, black dots), were selected

as the source locations for the water masses of the TSC and the Kuroshio, respectively. The particles  
480 were released on January 1, 2009 and tracked until March 31, 2009 (a total of 90 days).

Figure 15a shows the traces originating from the TSC area. Unlike the traditional route, where the TSC  
water flows from the Taiwan Strait to the inshore area between the 30 and 100 m isobaths, most particles  
(Fig. 15a, gray lines) were concentrated in the offshore branch under the effect of cross-shore fluctuation.  
485 Two particles were selected to show the inshore route (Fig. 15a, red line) and offshore route (Fig. 15a,  
blue line), with both passing the area north of Taiwan. When the two particles arrived at the area north  
of Taiwan, the behavior of the tracers, according to specific velocity conditions (Fig. 15c), was very  
different: a northwestward transport occurred on Jan. 25 for the inshore particles (Fig. 15c) and a  
northeastward transport occurred on Feb. 12 for the offshore particles (Fig. 15c). The velocity conditions  
490 in the area north of Taiwan corresponded to the variation of the Taiwan Strait flux (Fig. 10), which shows  
that the Taiwan Strait flux on Feb. 12 was much greater than on Jan. 25. Therefore, it can be concluded  
that the TSC intrusion induced an offshore transport north of Taiwan.

Figure 15b shows the traces originating from the Kuroshio area. In the same way as the TSC water, the  
495 Kuroshio water was also transported to the northern shelf via both the inshore branch and the offshore  
branch. The separation of the two branches north of Taiwan was caused by cross-shore fluctuations of  
the currents. When the two particles arrived at the area north of Taiwan, a northwestward transport  
occurred on Feb. 2 for the inshore particles (Fig. 15c) and a northeastward transport occurred on Feb. 12  
for the offshore particles (Fig. 15c). This means that the offshore transport induced by the TSC also had  
500 an effect on the distribution of Kuroshio water north of Taiwan. Liu et al. (2016) showed that the winter

TSC originated from a small branch of Kuroshio intrusion into the Luzon Strait. Our results complement this picture, since they show that most TSC particles flow into the TWC offshore branch under the influence of cross-shore fluctuation.

505

Figure 15

Our results may underestimate the impact of Kuroshio intrusion on the fluctuation of the TWC northeast of Taiwan, especially at the seasonal and interannual time scales. Wei et al. (2013) demonstrated that the annual and interannual variations of the Kuroshio volume transport are large. In addition, Zhou et al. (2015) pointed out that the annual and interannual variations of the Kuroshio intrusion northeast of Taiwan are prominent. Liu et al. (2014b) presented supportive evidence that the Kuroshio intrusion, from east of Taiwan to the onshore area north of Taiwan, is closely related to the Kuroshio volume transport. This relation between the Kuroshio intrusion and the Kuroshio volume transport had been interpreted by Su and Pan (1987) as the  $\beta$ -effect because of the sudden change in topography northeast of Taiwan. Our results show that the intra-seasonal variation of the Kuroshio intrusion and the Kuroshio volume transport was negligible compared with the TSC variation at the same time scale, indicating that the synoptic fluctuation of TWC north of Taiwan is mainly induced by the TSC. However, because FVCOM uses sigma co-ordinates in the vertical which are prone to errors in regions of steep topography, our results may underestimate the fluctuations at the shelf break, in particular to the northeast of Taiwan where Kuroshio intrusion occurs.

520



## 4.2 Water exchange in the inshore area induced by wind

In the inshore area, the synoptic fluctuations of the TWC (Fig. 9b) caused by wind were generally strong in the alongshore direction and regionally important (along the latitudes 26.5°N and 28°N) in the cross-shore direction. The alongshore fluctuations showed that the TWC inshore branch occurred episodically. This episodic occurrence of the TWC agrees with the results from a previous study based on four mooring surveys off the Zhe-Min coast (Zeng et al., 2012). The mechanism of the episodic occurrence of the TWC was mainly associated with the winter monsoon, which agrees with the analysis of observational data by Huang et al. (2016). However, the overall magnitude of the TWC fluctuation, and its role on the cross-shore flux, are still not fully understood due to the short-term nature of the observational data.

We investigated the magnitude of TWC fluctuation, and its role on the water exchange, in the inshore area. Previous studies (Su and Pan, 1987; Zeng et al., 2012) show that the TWC flows between the 50 and 100 m isobaths, whereas the ZMCC water dominates the coastal area west of the 50 m isobath in the surface layer. As mentioned when discussing Figure 9d, the strongest TWC could reach the coastal area as close as the 30 m isobath, being stronger than those reported in the literature. Moreover, the area with large fluctuations spanned the area between the 30 and 100 m isobaths (Fig. 9b), indicating that water exchange between the ZMCC water and the TWC water exists in the area between the 30 and 100 m isobaths.

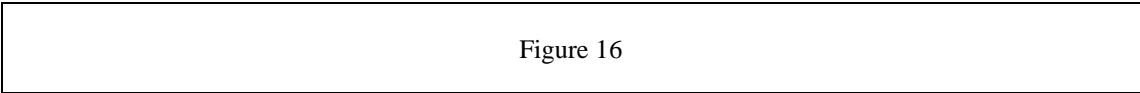
The episodic occurrence of the TWC inshore branch is directly related to the relative importance of the southwestward ZMCC (Fig. 16, blue arrows) and the northeastward TWC (Fig. 16, red arrows). In this paper, only wind-induced synoptic fluctuations are considered in the relations to the episodic events and

no short-term extreme storm events. When the winter monsoon (the northerly wind) prevails, the ZMCC  
545 occupies most of the inshore area and the TWC inshore branch weakens (Fig. 16a). On the contrary, the  
TWC inshore branch can intrude into the near-coast area under southerly wind conditions (Fig. 16b). The  
boundary between the coastal current and the TWC may shift from the 100 m isobaths to the 30 m isobath  
in the cross-shore direction, covering the entire area of the TWC inshore branch.

550 Our results further reveal that strong wind-induced cross-shore fluctuations occur in the inshore area (Fig.  
9f). This cross-shore fluctuation has a significant ecological impact because of the connected nutrient  
transport (Zhao and Guo, 2011). Ren et al. (2015) observed a cross-shore flux in the inshore area, which  
was triggered by the transition of northeasterly to southwesterly monsoonal winds. Their observed  
features can be further interpreted with our result that wind-induced fluctuations can affect the cross-  
555 shore water transport in the inshore area.

Largest cross-shore fluctuations were located at the latitudes 26.5 °N and 28 °N (Fig. 9f), which agreed  
well with the latitudes where the TWC offshore meanders occurred in the mean currents (Fig. 5a). This  
also indicates that the offshore transports were most significant along the latitudes 26.5 °N and 28 °N  
560 according to both the mean currents and the synoptic fluctuations. The offshore transport may be  
associated with the offshore-penetrating fronts of coastal water in the ECS. Many remote-sensing images  
(He et al. 2010; Bai et al. 2013) have exhibited offshore-penetrating fronts that crossed the 70 m isobath  
and played an important role in cross-shore material exchange, but the mechanisms of the offshore-  
penetrating fronts are still under debate. Yuan and Qiao (2005) pointed out that both downwelling- and  
565 upwelling-favorable winds are associated with the occurrence of the offshore-penetrating front. Ren et

al. (2015) suggested that the penetrating front is generated by the transition of northeasterly to southwesterly monsoonal winds. Wu (2015) suggested that the offshore-penetrating front is the response of buoyant coastal water to an along-isobath undulation of the ambient pycnocline, which is controlled by a temperature stratification of the water column. Our study offers a new interpretation, i.e., that the penetrating front is generated through the wind-induced fluctuations and the TWC offshore meanders.



## 575 **5 Conclusions**

The FVCOM model was able to reproduce the wintertime TWC in 2009 reasonably well, as shown by a validation in terms of the overall structure of the surface mean currents, the ECS boundary fluxes, and data from four mooring stations. The validation showed that the simulated TWC was comparable to the observed results, not only in terms of the mean currents but also in terms of the synoptic fluctuations.

580

The wintertime TWC showed two branches: one inshore and another offshore. The inshore branch covered an area between the 30 and 100 m isobaths and flowed northward via a straight route. The offshore branch was located between the 100 and 200 m isobaths and showed two prominent meanders.

It was shown that the Coriolis force was balanced by the pressure gradient in both branches, indicating

585 the dominant role of the geostrophic balance for the mean current in both branches.

Two regions with significant synoptic fluctuations, north of Taiwan and the inshore area, were

investigated using the EOF method. The first two leading modes explained 91% of the total variance.

EOF1 showed that fluctuations occurred in the cross-shore direction south of 26°N. These fluctuations

590 were mainly associated with variation of the TSC flux. EOF2 showed significant fluctuation between the 30 and 100 m isobaths. These fluctuations caused the episodic existence of the TWC inshore branch in the alongshore direction and cross-shore fluctuations mainly at latitudes 26.5°N and 28°N, which were mainly associated with the variation of wind speed.

595 We also studied the different dynamic reasons for the fluctuations in the two regions. In the area north of Taiwan, the TSC and Kuroshio converged to initiate the TWC. A barotropic pressure anomaly was generated by TSC intrusion from the Taiwan Strait causing a barotropic pressure gradient in the alongshore direction; this explains why the synoptic fluctuations in this area occurred in the cross-shore direction. Additionally, the wind had a strong effect on the synoptic fluctuations in the inshore area. The

600 northeasterly monsoon enhanced the southwestward ZMCC and replaced the TWC in the inshore area. This situation is reversed during the southwest monsoon.

The synoptic fluctuations north of Taiwan and in the inshore area are important for both the alongshore and cross-shore transports. Due to the fluctuation north of Taiwan, the mixed water of the TSC and the

605 Kuroshio was transported to both the inshore area and the offshore area, whereas most Taiwan Strait water was transported to the offshore area in winter. The inshore fluctuation not only caused an episodic occurrence of the TWC in the alongshore direction, which affected the alongshore transport of ZMCC water and TWC water between the 30 and 100 m isobaths, but also impacted the cross-shore transports along latitudes 26.5°N and 28°N.

### Acknowledgement

This study was jointly supported by the Sino-German cooperation in ocean and polar research under the grant BMBF-03F0701A (CLIFLUX), the National Natural Science Foundation of China (41306025, 41276028, 41321004) and the project of State Key Laboratory of Satellite Ocean Environment Dynamics, the Second Institute of Oceanography (SOEDZZ1512).

### References

- Bai, Y., Pan, D., Cai, W. J., He, X., Wang, D., Tao, B., and Zhu, Q.: Remote sensing of salinity from satellite-derived CDOM in the Changjiang River dominated East China Sea, *J. Geophys. Res. Ocean*, 118, 227–243, 2013.
- Bleck, R.: An oceanic general circulation model framed in hybrid isopycnic-Cartesian coordinates, *Ocean Model.*, 37, 55–88, 2002.
- Brink, K. H.: Costal trapped waves and wind-induced currents over the continental shelf, *Annual Review of Fluid Mechanics*, 23, 389–412, 1991.
- Carnes, M. R.: Description and evaluation of GDEM-V3.0, NRL Rep. NRL/MR/7330-09-9165, Nav. Res. Lab., Washington, D. C, 2009.
- Chen, C., Liu, H., and Beardsley, R. C.: An unstructured, finite-volume, three-dimensional, primitive equation ocean model: application to coastal ocean and estuaries, *J. Atm. Oceanic Tech.*, 20, 159–186, 2003.
- Chen, C., Beardsley, R. C., Limeburner, R., and Kim, K.: Comparison of winter and summer hydrographic observations in the Yellow and East China seas and adjacent Kuroshio during 1986, *Cont. Shelf Res.*, 14, 909–929, 1994.
- Chen, C., Xue, P., Ding, P., Beardsley, R. C., Xu, Q., Mao, X., Gao, G., Qi, J., Li, C., Lin, H., Cowles, G., and Shi, M.: Physical mechanisms for the offshore detachment of Changjiang Diluted Water in the East China Sea, *J. Geophys. Res.*, 113, C02002, doi:10.1029/2006JC003994, 2008.
- Chen, C. T. A. and Wang, S. L.: Carbon, alkalinity and nutrient budget on the East China Sea continental shelf, *J. Geophys. Res. Ocean*, 104, 20675–20686, 1999.
- Chuang, W. S. and Liang, W. D.: Seasonal variability of intrusion of the Kuroshio water across the continental shelf northeast of Taiwan, *J. Oceanogr.*, 50(5), 531–542, 1994.
- Cui, M., Hu, D., and Wu, L.: Seasonal and intraseasonal variations of the surface Taiwan Warm Current, *Chin. J. Oceanol. Limnol.*, 22, 271–277, 2004.
- Egbert, G. D., Bennett, A., and Foreman, M.: TOPEX/Poseidon tides estimated using a global inverse model, *J. Geophys. Res.* 99, 24821–24852, doi: 10.1029/94JC01894, 1994.
- Egbert, G. D. and Erofeeva, S. Y.: Efficient inverse modeling of barotropic ocean tides, *J. Atmos. Oceanic*

Technol., 19, 183–204, 2002.

Emery, W. J. and Thomson, R. E.: Data analysis methods in physical oceanography, Second and revised version, 658 pp., Elsevier Science B.V., Amsterdam, The Netherlands, 2001.

650 Fang, G., Zhao, B., and Zhu, Y.: Water volume transport through the Taiwan Strait and the continental shelf of the East China Sea measured with current meters, in *Oceanography of Asian Marginal Seas*, edited by K. Takano, 345–358pp., doi:10.1016/S0422-9894(08)70107-7, Elsevier, New York, 1991.

Feng, M., Mitsudera, H., and Yoshikawa, Y.: Structure and Variability of the Kuroshio Current in Tokara Strait, *J. Phys. Oceanogr.*, 30(9), 2257–2276, 2000.

Godin, G.: *The Analysis of Tides*, 264 pp., University of Toronto Press, Toronto, 1972.

655 Grachev, A. A., Andreas, E. L., Fairall, C. W., Guest, P. S., and Persson, P. O. G.: The critical Richardson number and limits of applicability of local similarity theory in the stable boundary layer, *Boundary-layer meteorology*, 147(1), 51–82, 2013.

Guan, B. and Fang, G.: Winter counter-wind currents off the southeastern China coast: A review, *J. Oceanogr.*, 62, 1–24, 2006.

660 Guan, B. and Mao, H.: A note on circulation of the East China Sea, *Chin. J. Oceanol. Limnol.*, 1, 5–16, 1982.

Guan, B. X.: A sketch of the current system of the East China Sea, in *Collected Papers of the Continental Shelf of the East China Sea* (in Chinese), 126–133pp., Inst. of Oceanol., Chin. Acad. of Sci., Qingdao, China, 1978.

665 Guo, X. Y., Hukuda, H., Miyazawa, Y., and Yamagata, T.: A triply nested ocean model for simulating the Kuroshio - Roles of horizontal resolution on JEBAR, *J. Phys. Oceanogr.*, 33, 146–169, 2003.

Guo, X. Y., Miyazawa, Y., and Yamagata, T.: The Kuroshio onshore intrusion along the shelf break of the East China Sea: The origin of the Tsushima Warm Current, *J. Phys. Oceanogr.*, 36, 2205–2231, doi:10.1175/JPO2976.1, 2006.

670 He, L., Li, Y., Zhou, H., and Yuan, D.: Variability of cross-shelf penetrating fronts in the East China Sea, *Deep Sea Res.*, 57, 1820–1826, 2010.

Hong, H., Chai, F., Zhang, C., Huang, B., Jiang, Y., and Hu, J.: An overview of physical and biogeochemical processes and ecosystem dynamics in the Taiwan Strait, *Cont. Shelf Res.*, 31, 3–12, 2011.

675 Hsin, Y. C., Qiu, B., Chiang, T. L., and Wu, C. R.: Seasonal to interannual variations in the intensity and central position of the surface Kuroshio east of Taiwan, *J. Geophys. Res. Oceans*, 118(9), 4305–4316, 2013.

Hu, J., Kawamura, H., Li, C., Hong, H., and Jiang, Y.: Review on current and seawater volume transport through the Taiwan Strait, *J. Oceanogr.*, 66, 591–610, 2010.

680 Huang, D., Zeng, D., Ni, X., Zhang, T., Xuan, J., Zhou, F., Li, J., and He, S.: Alongshore and cross-shore circulations and their response to winter monsoon in the western East China Sea, *Deep-Sea Res. II*, 124, 6–18, <http://dx.doi.org/10.1016/j.dsr2.2015.01.001i>, 2016,

Hung, J. J., Chen, C. H., Gong, G. C., Sheu, D. D., and Shiah, F. K.: Distributions, stoichiometric patterns and cross-shelf exports of dissolved organic matter in the East China Sea, *Deep-Sea Res. II*, 50, 1127–1145, 2003.

685 Huthnance, J. M., Mysak, L. A., and Wang, D. P.: Coastal trapped waves, in: Mooers C.N.K. (ed.) *Baroclinic Processes on Continental Shelves*. Coastal and Estuarine Sciences, 3, pp. 1–18. Washington DC, American Geophysical Union, 1986.

Huyer, A.: Shelf circulation, In Mehaute, B. L., Hames, D. M. (Eds.), *The Sea, Volume 9: Ocean*

- 690 Engineering Science, Wiley, pp. 423–466, 1990.
- Isobe, A.: Recent advances in ocean-circulation research on the Yellow Sea and East China Sea shelves, *J. Oceanogr.*, 64, 569–584, doi:10.1007/s10872-008-0048-7, 2008.
- Johns, W. E., Lee, T. N., Zhang, D., Zantopp, R., Liu, C. T., and Yang, Y.: The Kuroshio east of Taiwan: Moored transport observations from the WOCE PCM-1 array, *J. Phys. Oceanogr.*, 31(4), 1031–1053, 695 2001.
- Ledwell, J. R., Watson, A. J., and Law, C. S.: Mixing of a tracer in the pycnocline, *J. Geophys. Res.*, 103(C10), 21499–21529, doi:10.1029/98JC01738, 1998.
- Lee, J. S. and Matsuno, T.: Intrusion of Kuroshio water onto the continental shelf of the East China Sea, *J. Oceanogr.*, 63, 309–325, 2007.
- 700 Liu, C., Wang, F., Chen, X., and VonStorch, J. S.: Interannual variability of the Kuroshio onshore intrusion along the East China Sea shelf break: Effect of the Kuroshio volume transport, *J. Geophys. Res. Oceans*, 119, 6190–6209, doi:10.1002/2013JC009653, 2014a.
- Liu, T., Xu, J., He, Y., Lü, H., Yao, Y., and Cai, S.: Numerical simulation of the Kuroshio intrusion into the South China Sea by a passive tracer, *Acta Oceanologica Sinica*, 35(9): 1–12, doi: 705 10.1007/s13131-016-0930-x, 2016.
- Liu, X., Dong, C., Chen, D., and Su, J.: The pattern and variability of winter Kuroshio intrusion northeast of Taiwan, *J. Geophys. Res. Oceans*, 119, 5380–5394, DOI 10.1002/2014JC009879, 2014b.
- Mellor, G. L. and Durbin, P. A.: The structure and dynamics of the ocean surface mixed layer, *J. Phys. Oceanogr.*, 5(4), 718–728, 1975.
- 710 Oey, L. Y., Hsin, Y. C., and Wu, C. R.: Why does the Kuroshio northeast of Taiwan shift shelfward in winter?, *Ocean Dynam.*, 60(2), 413–426, 2010.
- Qiu, B. and Imasato, N.: A numerical study on the formation of the Kuroshio countercurrent and the Kuroshio Branch Current in the East China Sea, *Cont. Shelf Res.*, 10, 165–184, doi:10.1016/0278-4343(90)90028-K, 1990.
- 715 Ren, J. L., Xuan, J., Wang, Z. W., Huang, D., and Zhang, J.: Cross-shelf transport of terrestrial Al enhanced by the transition of northeasterly to southwesterly monsoon wind over the East China Sea, *J. Geophys. Res. Oceans*, 120, doi:10.1002/2014JC010655, 2015.
- Richardson, H., Basu, S., and Holtslag, A. A. M.: Improving stable boundary-layer height estimation using a stability-dependent critical bulk Richardson number, *Boundary-layer meteorology*, 148(1), 720 93–109, 2013.
- Smith, W. H. F. and Sandwell, D. T.: Global sea floor topography from satellite altimetry and ship depth soundings, *Science*, 277, 1956–1962, 1997.
- Su, J. L. and Pan, Y. Q.: On the shelf circulation north of Taiwan, *Acta Oceanol. Sin.*, 6, 1–20, 1987.
- Su, J. L., Pan, Y. Q., and Liang, X. S.: Kuroshio intrusion and Taiwan warm current, *Oceanology of 725 China Seas*. Springer Netherlands, 59–70, 1994.
- Takahashi, D. and Morimoto, A.: Mean field and annual variation of surface flow in the East China Sea as revealed by combining satellite altimeter and drifter data, *Prog. Oceanogr.*, 111, 125–139, doi: 10.1016/j.pocean.2013.01.007, 2013.
- Teague, W., Jacobs, G., Ko, D., Tang, T., Chang, K. I., and Suk, M. S.: Connectivity of the Taiwan, Cheju, and Korea straits, *Conti. Shelf Res.*, 23(1), 63–77, 2003.
- 730 Uppala, S. M., Kållberg, P. W., Simmons, A. J., Andrae, U., Bechtold, V. D. C., Fiorino, M., Gibson, J. K., Haseler, J., Hernandez, A., Kelly, G. A., Li, X., Onogi, K., Saarinen, S., Sokka, N., Allan, R. P., Andersson, E., Arpe, K., Balmaseda, M. A., Beljaars, A. C. M., Berg, L. V. D., Bidlot, J., Bormann,

- 735 N., Caires, S., Chevallier, F., Dethof, A., Dragosavac, M., Fisher, M., Fuentes, M., Hagemann, S.,  
H m, E., Hoskins, B. J., Isaksen, L., Janssen, P. A. E. M., Jenne, R., McNally, A. P., Mahfouf, J.-F.,  
Morcrette, J.-J., Rayner, N. A., Saunders, R. W., Simon, P., Sterl, A., Trenberth, K. E., Untch, A.,  
Vasiljevic, D., Viterbo, P., and Woollen, J.: The ERA-40 re-analysis, *Q. J. R. Meteorol. Soc.*, 131,  
2961–3012. doi:10.1256/qj.04.176, 2005.
- 740 Wang, Y., Jan, S., and Wang, D.: Transports and tidal current estimates in the Taiwan Strait from  
shipboard ADCP observations (1999–2001), *Estuarine Coastal Shelf Sci.*, 57(1), 193–199, 2003.
- Wei, Y., Huang, D., and Zhu, X. H.: Interannual to decadal variability of the Kuroshio Current in the east  
china sea from 1955 to 2010 as indicated by in-situ hydrographic data, *J. Oceanogr.*, 69(5), 571–  
589, 2013.
- 745 Wu, H.: Cross-shelf penetrating fronts: A response of buoyant coastal water to ambient pycnocline  
undulation, *J. Geophys. Res.*, 120, doi:10.1002/2014JC010686, 2015.
- Wu, C. R. and Hsin, Y. C.: Volume transport through the Taiwan Strait: a numerical study, *Terr. Atmos.*  
*Ocean. Sci.*, 16(2), 377–391, 2005.
- Xuan, J., Huang, D., Zhou, F., Zhu, X. H., and Fan, X.: The role of wind on the detachment of low salinity  
water in the Changjiang Bank in summer, *J. Geophys. Res. Ocean*, 117, C10004, doi:  
750 10.1029/2012JC008121, 2012.
- Xuan, J., Yang, Z., Huang, D., Wang, T., and Zhou, F.: Tidal residual current and its role in the mean flow  
on the Changjiang Bank, *J. Mar. Syst.*, 154, 66–81, doi: 10.1016/j.jmarsys.2015.04.005, 2016.
- Xuan, J., Zhou, F., Huang, D., Zhu, X. H., Xing, C., and Fan, X.: Modelling the timing of major spring  
bloom events in the central Yellow Sea, *Estuarine Coastal Shelf Sci.*, 113, 283–292, 2012.
- 755 Yang, D., Yin, B., Liu, Z., and Feng, X.: Numerical study of the ocean circulation on the East China Sea  
shelf and a Kuroshio bottom branch northeast of Taiwan in summer, *J. Geophys. Res. Ocean*, 116,  
C05015, doi:10.1029/2010JC006777, 2011.
- Yang, D., Yin, B., Liu, Z., Bai, T., Qi, J., and Chen, H.: Numerical study on the pattern and origins of  
Kuroshio branches in the bottom water of southern East China Sea in summer, *J. Geophys. Res.*  
760 *Ocean*, 117, C02014, doi:10.1029/2011JC007528, 2012.
- Yu, L. and Weller, R. A.: Objectively Analyzed air–sea heat Fluxes (OAFlux) for the global oceans, *B.*  
*Am. Meteorol. Soc.* 88, 527–539, 2007.
- Yuan, D., Qiao, F., and Su, J.: Cross-shelf penetrating fronts off the southeast coast of China observed by  
MODIS. *Geophys. Res. Lett.*, 32, L19603, doi:10.1029/2005GL023815, 2005.
- 765 Zeng, D. Y., Ni, X., and Huang, D.: Temporal and spatial variability of the Zhe-Min Coastal Current and  
the Taiwan Warm Current in winter in the southern Zhejiang coastal sea, *Sci. Sin. Terrae.*, 42, 1123–  
1134, 2012.
- Zhao, L. and Guo, X.: Influence of cross-shelf water transport on nutrients and phytoplankton in the East  
China Sea: A model study, *Ocean Sci.*, 7, 27–43, doi:10.5194/os-7-27-2011, 2011.
- 770 Zhou, F., Xue, H., Huang, D., Xuan, J., Ni, X., Xiu, P., and Hao, Q.: Cross shelf exchange in the shelf of  
the East China Sea, *J. Geophys. Res. Oceans*, 120, 1545–1572, doi:10.1002/2014JC010567, 2015.
- Zhu, J., Chen, C., Ding, P., Li, C., and Lin, H.: Does the Taiwan Warm Current exist in winter?, *Geophys.*  
*Res. Lett.*, 31, L12302, doi:10.1029/2004GL019997, 2004.

### Table Captions

- 775 Table 1: Annual-mean volume transports ( $S_v = 10^6 \text{ m}^3/\text{s}$ ) through various sections. The sections are



shown in Figure 2 using blue dashed lines.

### Figure Captions

780 Figure 1: Density ( $\sigma_t$ ,  $\text{kg/m}^3$ ) distributions at 50 m depth derived the GDEM climatological data in February (a), an ocean survey from Feb. 1–27, 2007 (b), and an ocean survey from Feb. 3–16, 2007 (c), with the density anomalies between the GDEM data and the two surveys (d and e). The two blue arrows indicate the two TWC branches in winter. The 30, 50, 70, 100 and 200 m isobaths are indicated with grey lines in panel a.

785 Figure 2: The FVCOM model grid (Left) and the surface mean flow in the ECS in winter (Right). The colors in the left panel show the grid length (km). The letters a, b, and c indicate the three open boundaries at the Taiwan Strait, the northwest Pacific Ocean, and the Japan/East Sea, respectively. The blue dashed lines show some important straits around shelf boundary, including the Taiwan Strait (TWS), the East Taiwan Channel (ET), the Tsushima Strait (TUS), the Tokara Strait (TOS), and shelf break at the 200 m  
790 isobath. The red rectangle shows the study area of the wintertime TWC. The four red numbers off the Zhe-Min coast shows the four mooring sites observed from Jan. 5 to Feb. 28, 2009.

Figure 3: Validations of the wintertime TWC (warm color) along the section off the Zhe-Min coast (the short line with four red numbers in Figure 2): (a) observed alongshore currents; (b) simulated alongshore  
795 currents; (c) observed cross-shore currents; (d) simulated cross-shore currents. Note, an enlarged color scale is used for the cross-shore component to have a clear view of its weak structure.

Figure 4: Validations of the wintertime TWC fluctuations: (a) observed alongshore currents; (b) simulated alongshore currents; (c) observed cross-shore currents; (d) simulated cross-shore currents. The observation data comes from Station 4 in Figure 1 and the simulated data has the same position and period as the observation data.

Figure 5: a) Distribution of flow axes in the ECS in winter. The black arrows show the maximum velocity (m/s) in the vertical profile (VMV) and the color shows the speed of the VMV. The two blue arrows with label IB and OB represent the flow axes of the inshore branch and offshore branch, respectively. The red line DL1 represents the dividing line between the coastal current and inshore branch, and the red line DL2 separates the two TWC branches. b) Depth (m) of flow axes in the ECS. Sections S1–S6 were selected to study the wintertime TWC. c) Flux of inshore branch (blue) and offshore branch (red) at different latitudes. Dashed lines show the positions of Sections. S1–S6. Note, the scale is not linear.

Figure 6: Distributions of current speed along the six sections S1–S6 in winter. The blue arrow on the left indicates the inshore branch according to the velocity cores from section S3 to S6. The blue arrow on the right indicates the offshore branch according to the velocity cores from section S2 to S6. TSC is the Taiwan Strait Warm Current.

Figure 7: Current standard deviation in the layer of the VMV. The color shading shows the magnitude of the current standard deviation. The two blue arrows indicate the two TWC branches. The red curve indicate the area where the current standard deviation is larger than 0.1 m/s and their representative points (P1 and P2) are selected for later analysis.

820

Figure 8: Variation of alongshore currents (m/s) for the entire water column north of Taiwan (P1) and in the inshore area (P2) and their relation with upper mixed layer depth. The positive velocity (warm color) indicates the occurrence of the TWC. The gray solid lines show the depth of the upper mixed layer.

825 Figure 9: The spatial pattern of the first (EOF1; left) and second (EOF2; right) leading modes of the VMV in the ECS: (a) EOF1 currents, (b) EOF2 currents, (c) EOF1 alongshore component, (d) EOF2 alongshore component, (e) EOF1 cross-shore component, and (f) EOF2 cross-shore component. The 30, 50, 70, 100 and 200 m isobaths are indicated with grey lines.

830 Figure 10: Temporal variation of EOF1, north-south component of wind speed, surface net heat flux, and TSC flux along the TWS section, and Kuroshio flux along the ET section. Their linear correlation coefficients  $R$  and time-lags are also indicated in each panel. The  $p$  value is a declining indicator which indicates the impact significance of the linear correlation coefficients  $R$  whereby  $R$  has statistical significance and the confidence level is larger than 95% when the  $p$  value is less than 0.05.

835

Figure 11: Temporal variation of EOF2, north-south component of wind speed, surface net heat flux, and TSC flux along the TWS section, and Kuroshio flux along the ET section. Their linear correlation coefficients and time-lags are also indicated in each panel.

840 Figure 12: The effects of Coriolis force (a), total pressure (b), surface friction (c), bottom friction (d), advection (e), and local acceleration (f) for water column in winter according to Eq. (5) (units:  $10^{-4}$

m<sup>2</sup>/s<sup>2</sup>). The two blue arrows indicate the two TWC branches. The two triangles indicate the two regions with significant fluctuation north of Taiwan (P1) and in the inshore area (P2).

845 Figure 13: Variations in Coriolis force, total pressure, and wind in the alongshore direction at P1 (a), the cross-shore direction at P1 (b), the alongshore direction at P2 (c), and the cross-shore direction at P2 (d) according to Eq. (5).

Figure 14: Mean currents (upper panels) and synoptic fluctuations (EOF1 in middle panels and EOF2 in 850 bottom panels) in winters of 2010-2013. The black arrows show the velocity (m/s) in the layer of VMV and the color shows the current speed. The two blue arrows with label IB and OB represent the flow axes of the inshore branch and offshore branch, respectively.

Figure 15: Traces of TSC water (a) and Kuroshio water (b) in winter, with the variation of surface currents 855 at the original location of P1 (c). The black dots represent the release locations of tracers. The gray lines show the entire trajectories of the tracers. The red lines and blue lines are selected trajectories, which are close to the inshore branch and offshore branch, respectively. The dates show the times that selected tracers reached the origin location P1; note that the location of P1 is not fixed but varies with time. The numbers are the depths of the tracers, which are labeled at an interval of six days. The two black arrows 860 represent the two TWC branches.

Figure 16: The VMV under the northerly wind (a) and southerly wind (b). Panel (c) shows the variation of wind in winter. Blue vectors and red vectors show the southwestward coastal current and the

northeastward TWC, respectively. Gray contours indicate the 30, 50, 70, and 100 m isobaths. The two  
865 black arrows represent the two TWC branches. The green ellipse indicates the inshore area with  
significant fluctuation.

Table 1: Annual-mean volume transports ( $S_v = 10^6 \text{ m}^3/\text{s}$ ) through various sections. The sections are shown in Figure 2 using blue dashed lines.

Section	Present model	Previous estimates
<b>Taiwan Strait</b>	1.22	1.2 (Isobe, 2008)
		1.8 (Wang et al., 2003)
		1.09 (Wu and Hsin, 2005)
		1.03 (Yang et al., 2011)
		1.72 (Guo et al., 2006)
		0.5 (Hung et al., 2003)
		1.10 (Liu et al., 2014b)
<b>Tsushima Strait</b>	2.85	2.65 (Isobe, 2008)
		3.03 (Guo et al., 2006)
		2.70 (Yang et al., 2011)
		2.52 (Liu et al., 2014b)
<b>200m isobath</b>	1.66	1.46 (Guo et al., 2006)
		0.87 (Liu et al., 2014a)
		3.0 (Teague et al., 2003)
		2.74 (Lee and Matsuno, 2007)
<b>East Taiwan Channel</b>	22.71	21.50 (Johns et al., 2001)
		23.00 (Teague et al., 2003)
		23.83 (Guo et al., 2006)
		28.4 (Hsin et al., 2013)
		21.37 (Yang et al., 2011)
		20.74 (Liu et al., 2014b)
<b>Tokara Strait</b>	23.20	23.4 (Feng et al., 2000)
		20.00 (Teague et al., 2003)
		20.66 (Yang et al., 2011)
		24.42 (Liu et al., 2014b)

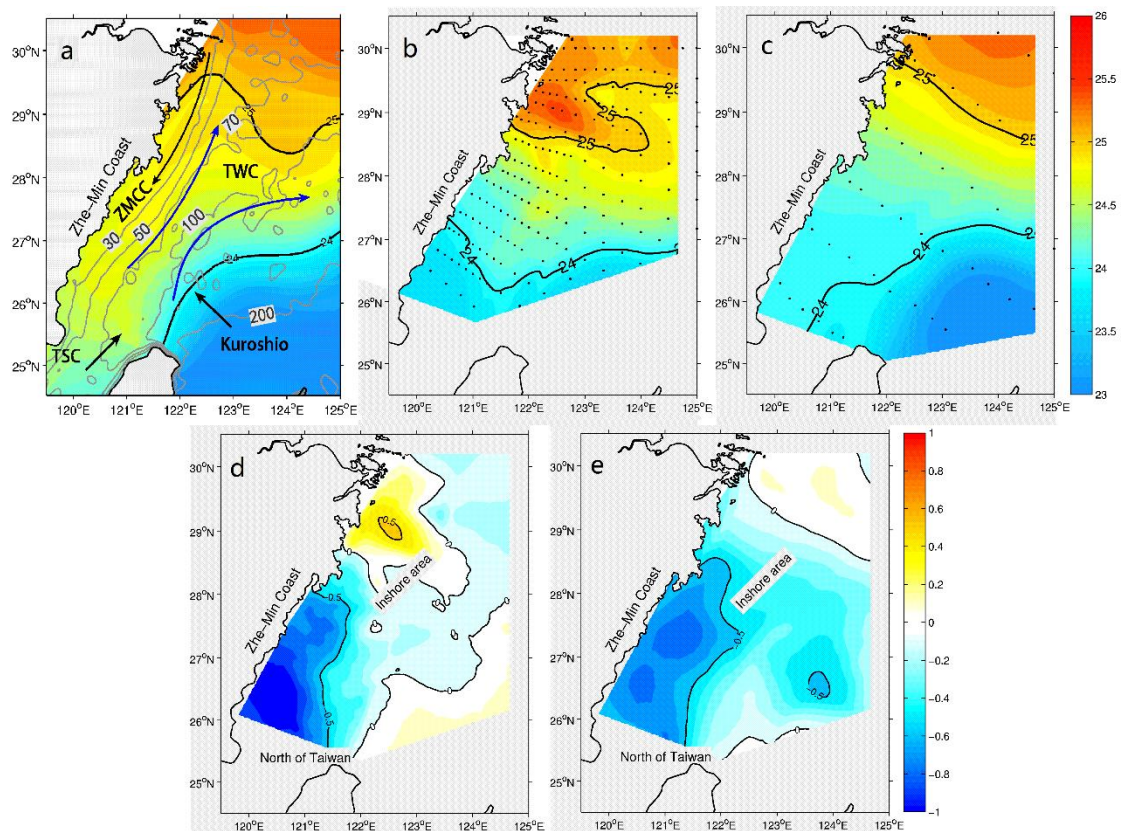
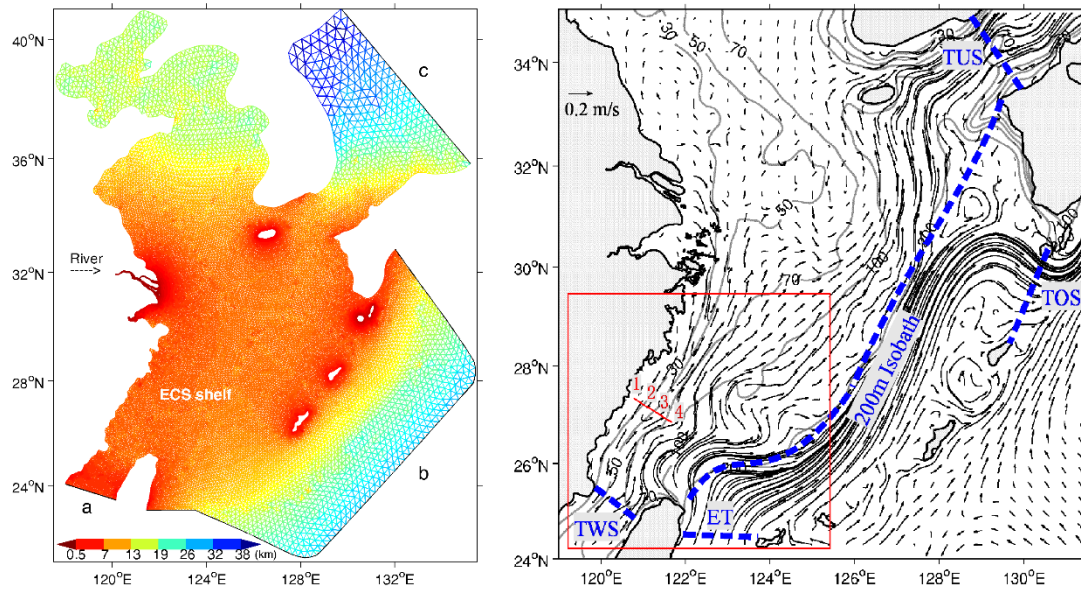


Figure 1: Density ( $\sigma_t$ ,  $\text{kg/m}^3$ ) distributions at 50 m depth derived the GDEM climatological data in February (a), an ocean survey from Feb. 1–27, 2007 (b), and an ocean survey from Feb. 3–16, 2007 (c), with the density anomalies between the GDEM data and the two surveys (d and e). The two blue arrows indicate the two TWC branches in winter. The 30, 50, 70, 100 and 200 m isobaths are indicated with grey lines in panel a.

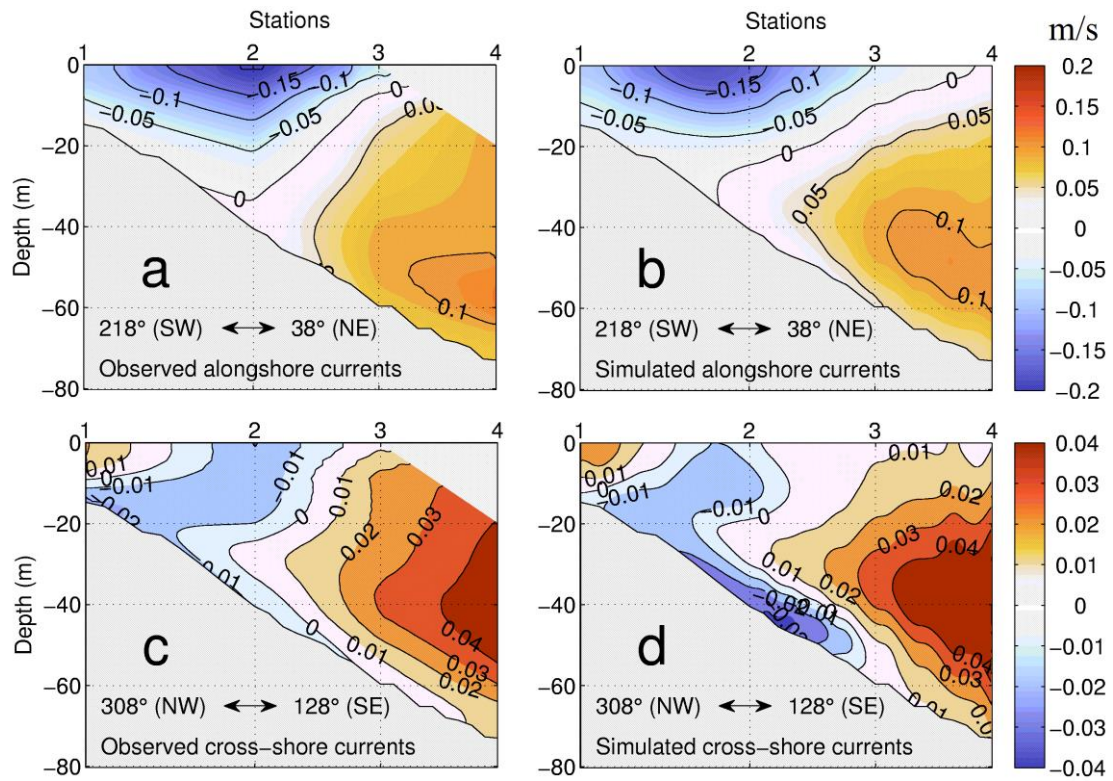


880

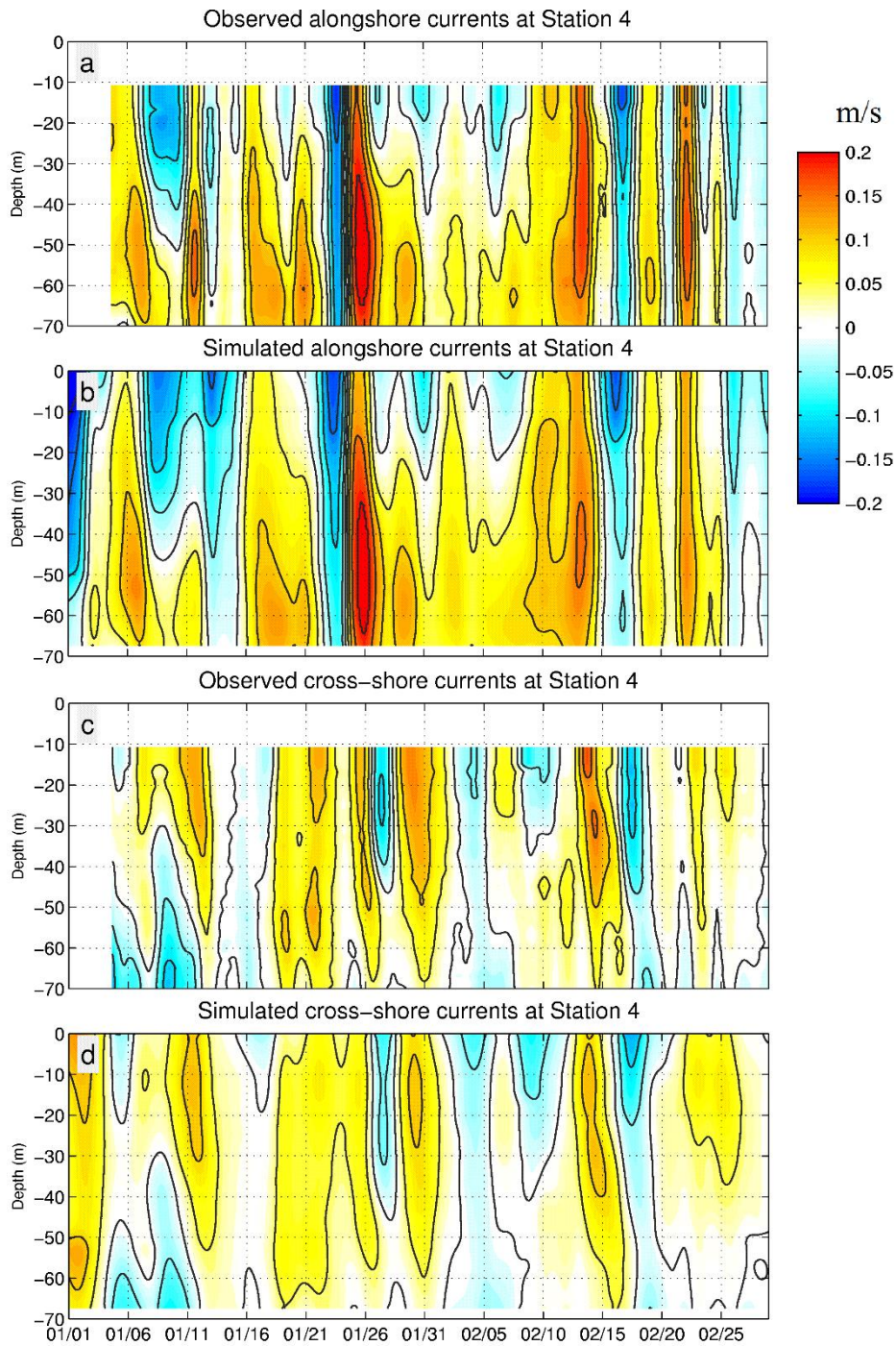
Figure 2: The FVCOM model grid (Left) and the surface mean flow in the ECS in winter (Right). The colors in the left panel show the grid length (km). The letters a, b, and c indicate the three open boundaries at the Taiwan Strait, the northwest Pacific Ocean, and the Japan/East Sea, respectively. The blue dashed lines show some important straits around shelf boundary, including the Taiwan Strait (TWS), the East Taiwan Channel (ET), the Tsushima Strait (TUS), the Tokara Strait (TOS), and shelf break at the 200 m isobath. The red rectangle shows the study area of the wintertime TWC. The four red numbers off the Zhe-Min coast shows the four mooring sites observed from Jan. 5 to Feb. 28, 2009.

885





890 Figure 3: Validations of the wintertime TWC (warm color) along the section off the Zhe-Min coast (the short line with four red numbers in Figure 2): (a) observed alongshore currents; (b) simulated alongshore currents; (c) observed cross-shore currents; (d) simulated cross-shore currents. Note, an enlarged color scale is used for the cross-shore component to have a clear view of its weak structure.



895

Figure 4: Variations of the inshore branch of TWC during January and February 2009: (a) observed alongshore currents; (b) simulated alongshore currents; (c) observed cross-shore currents; (d) simulated cross-shore currents. The observation data comes from Station 4 in Figure 1 and the simulated data has the same position and period as the observation data.

900

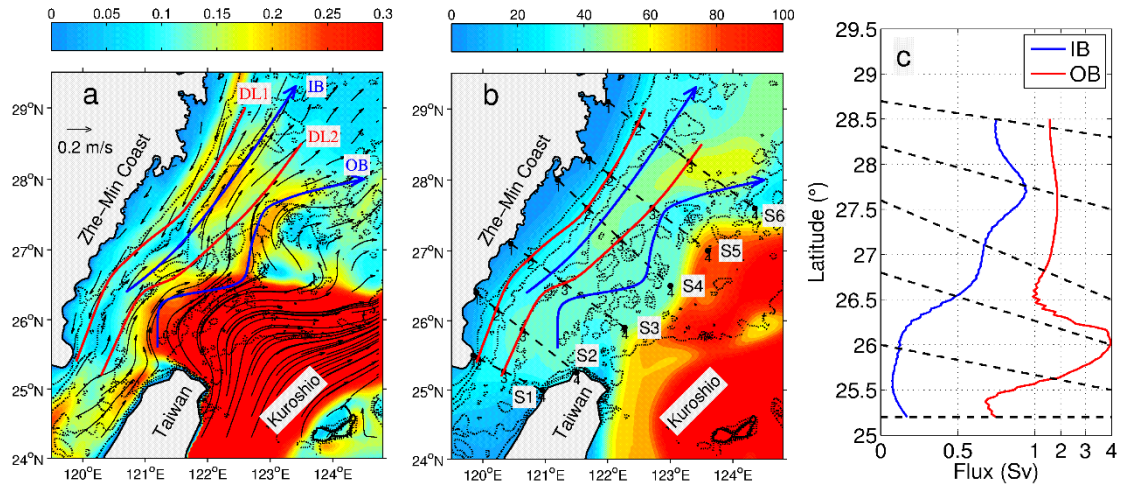
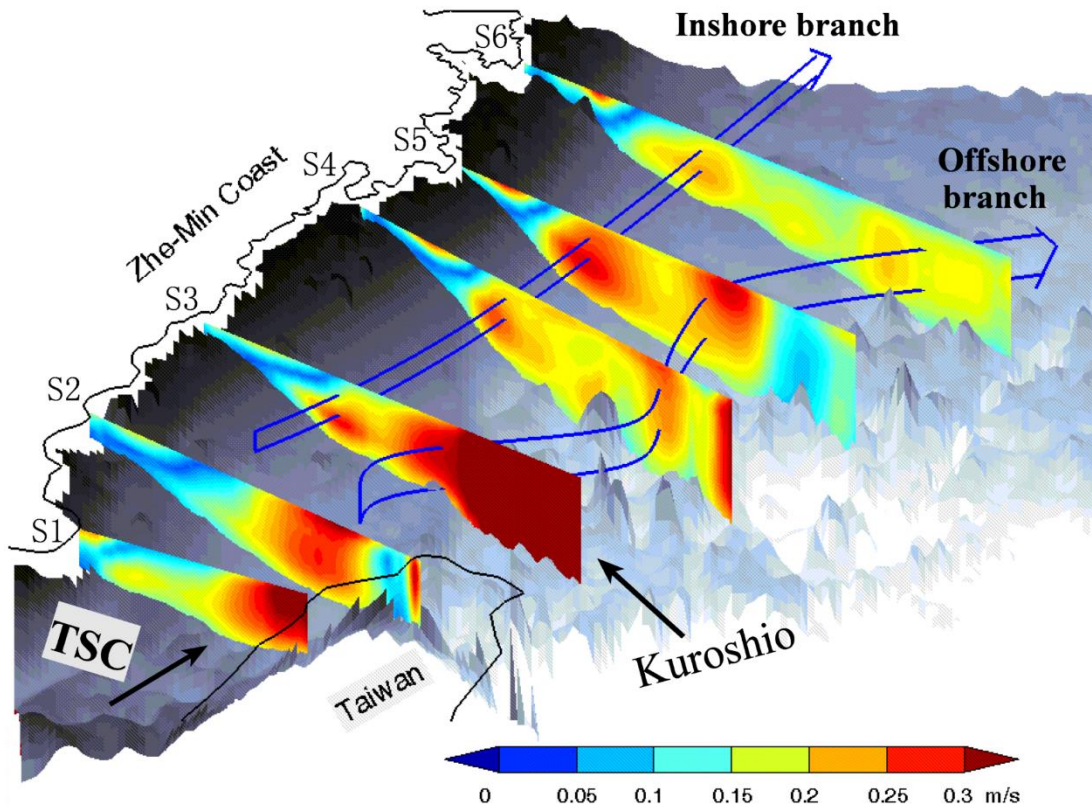


Figure 5: a) Distribution of flow axes in the ECS in winter. The black arrows show the maximum velocity (m/s) in the vertical profile (VMV) and the color shows the speed of the VMV. The two blue arrows with label IB and OB represent the flow axes of the inshore branch and offshore branch, respectively. The red line DL1 represents the dividing line between the coastal current and inshore branch, and the red line DL2 separates the two TWC branches. b) Depth (m) of flow axes in the ECS. Sections S1–S6 were selected to study the wintertime TWC. c) Flux of inshore branch (blue) and offshore branch (red) at different latitudes. Dashed lines show the positions of Sections. S1–S6. Note, the scale is not linear.





910

Figure 6: Distributions of current speed along the six sections S1–S6 in winter. The blue arrow on the left indicates the inshore branch according to the velocity cores from section S3 to S6. The blue arrow on the right indicates the offshore branch according to the velocity cores from section S2 to S6. TSC is the Taiwan Strait Current.

915

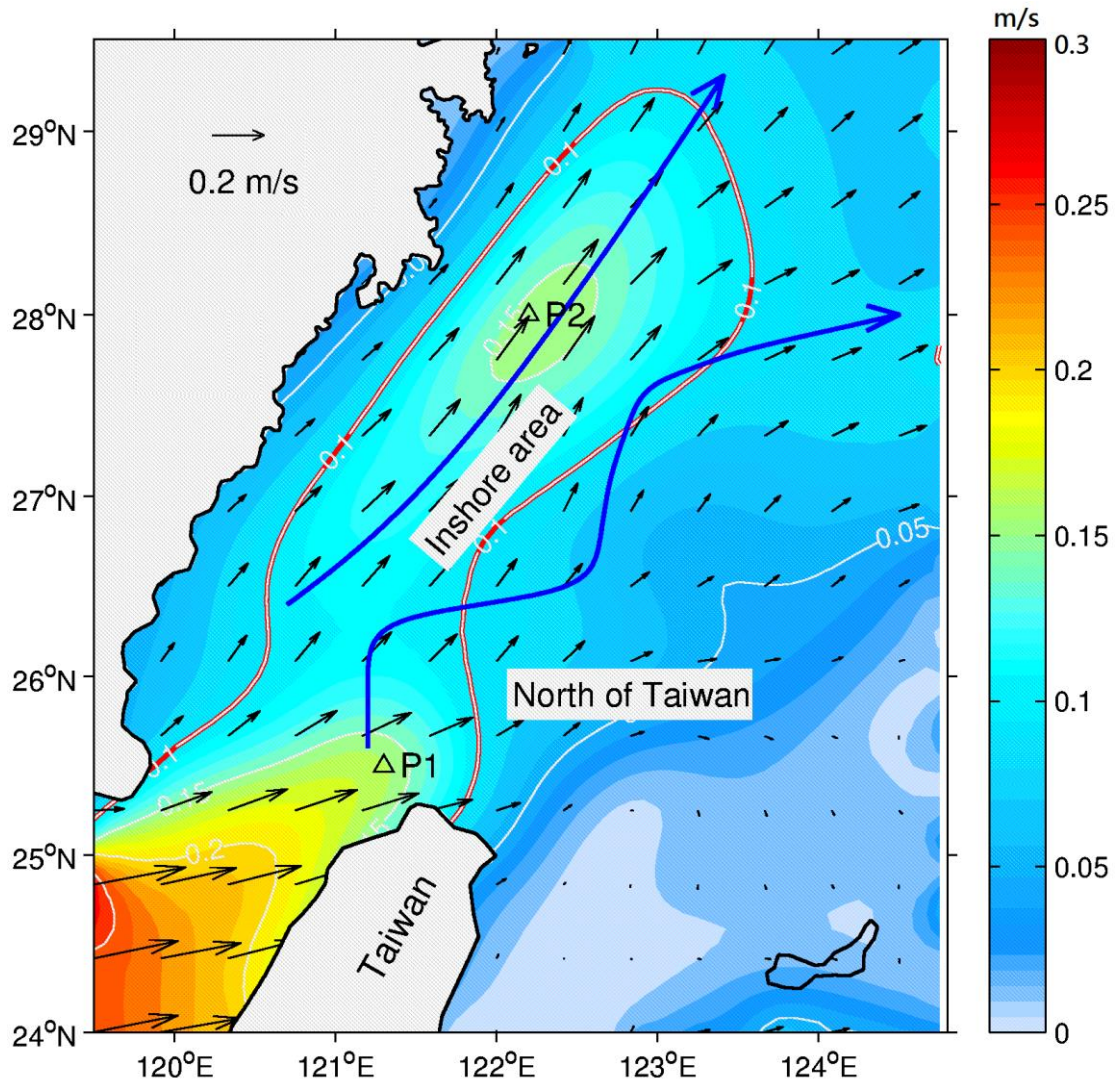


Figure 7: Current standard deviation in the layer of the VMV. The color shading shows the magnitude of the current standard deviation. The two blue arrows indicate the two TWC branches. The red curve indicate the area where the current standard deviation is larger than 0.1 m/s and their representative points

920 (P1 and P2) are selected for later analysis.

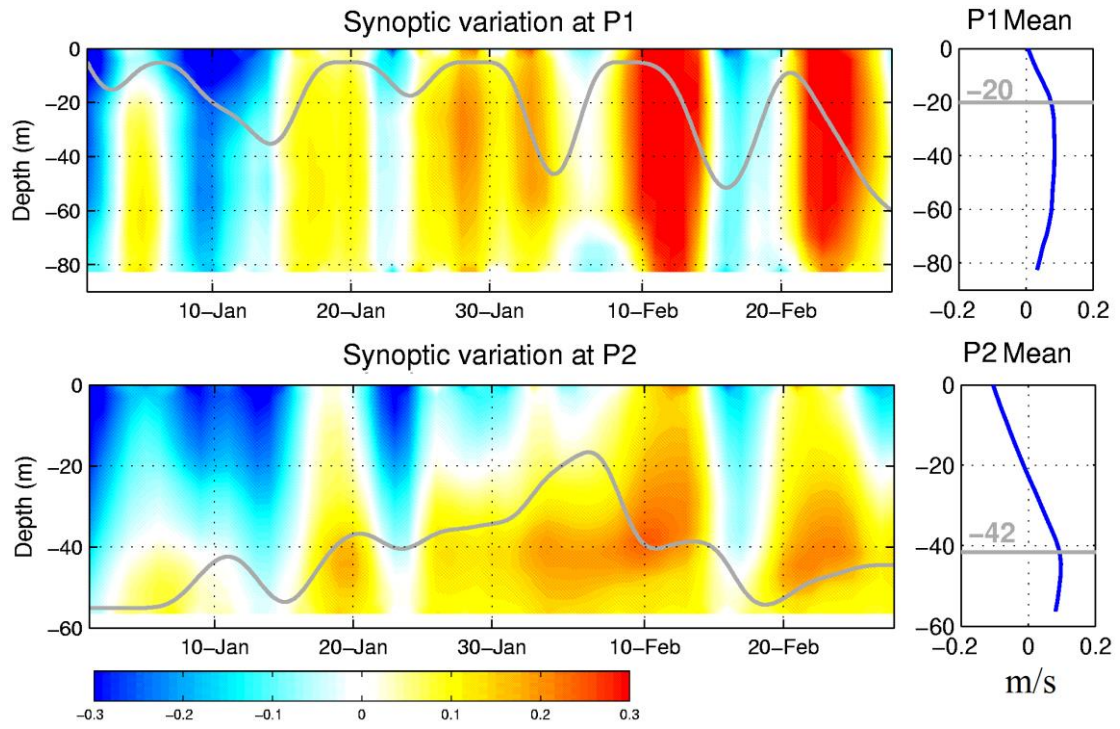


Figure 8: Variation of alongshore currents (m/s) for the entire water column north of Taiwan (P1) and in the inshore area (P2) and their relation with upper mixed layer depth. The positive velocity (warm color) indicates the occurrence of the TWC. The gray solid lines show the depth of the upper mixed layer.

925



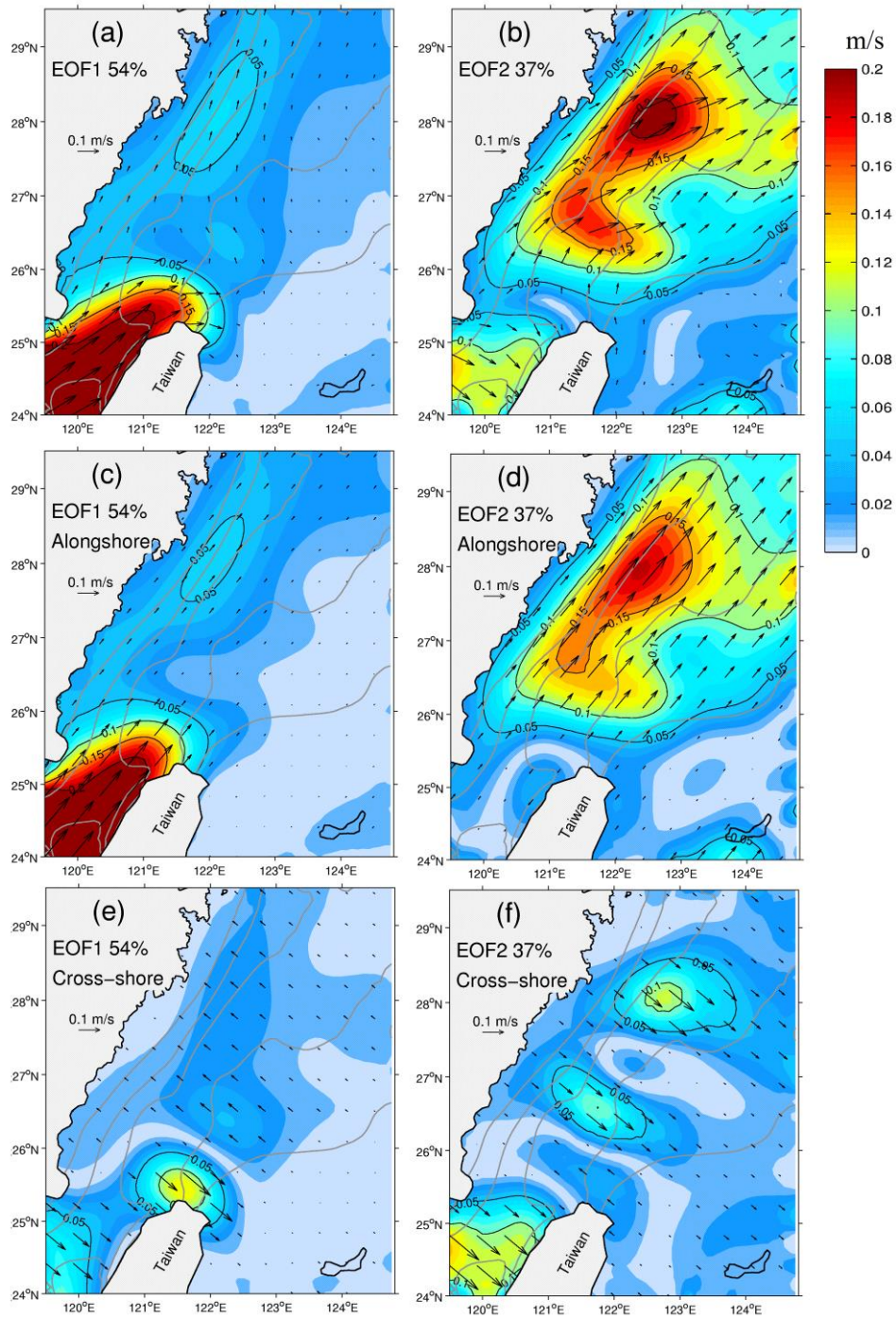


Figure 9: The spatial pattern of the first (EOF1; left) and second (EOF2; right) leading modes of the VMV in the ECS: (a) EOF1 currents, (b) EOF2 currents, (c) EOF1 alongshore component, (d) EOF2 alongshore component, (e) EOF1 cross-shore component, and (f) EOF2 cross-shore component. The 30, 50, 70, 100 and 200 m isobaths are indicated with grey lines.

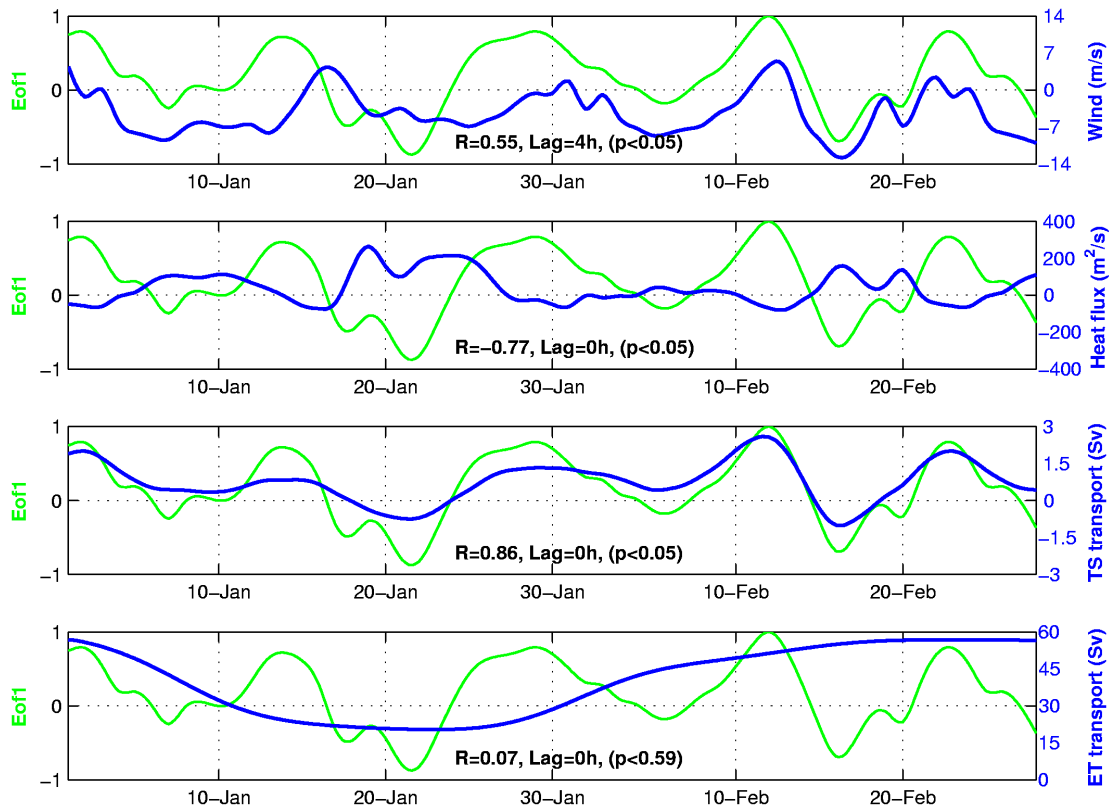
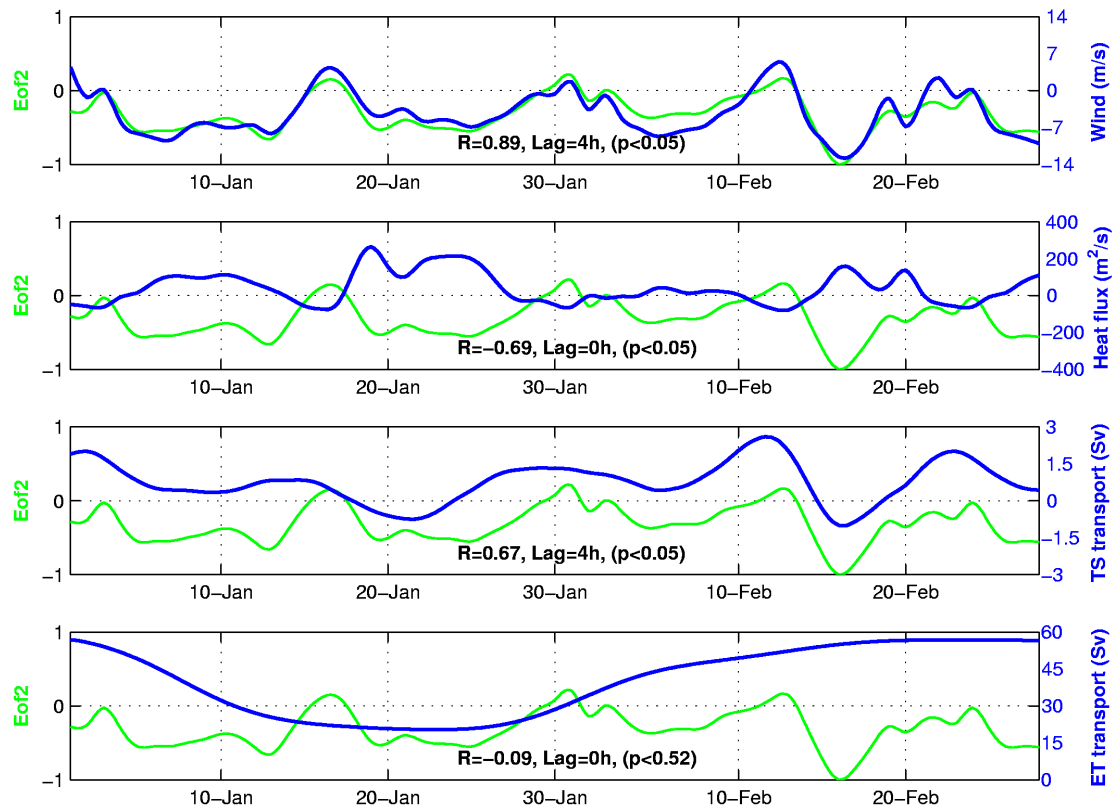


Figure 10: Temporal variation of EOF1, north-south component of wind speed, surface net heat flux, and

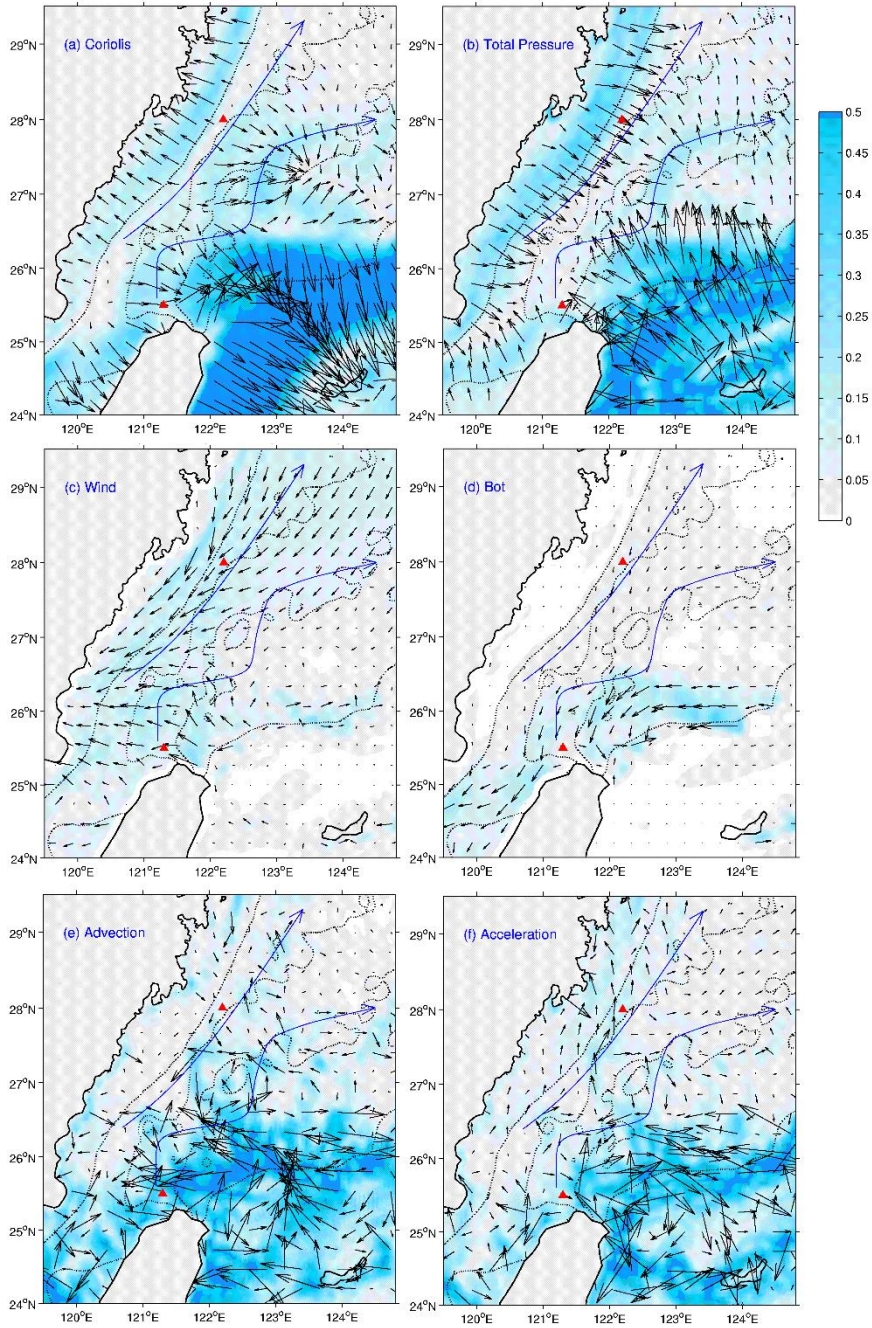
935 TSC flux along the TWS section, and Kuroshio flux along the ET section. Their linear correlation coefficients  $R$  and time-lags are also indicated in each panel. The  $p$  value is a declining indicator which indicates the impact significance of the linear correlation coefficients  $R$  whereby  $R$  has statistical significance and the confidence level is larger than 95% when the  $p$  value is less than 0.05.





940

Figure 11: Temporal variation of EOF2, north-south component of wind speed, surface net heat flux, and TSC flux along the TWS section, and Kuroshio flux along the ET section. Their linear correlation coefficients and time-lags are also indicated in each panel.



945

Figure 12: The effects of Coriolis force (a), total pressure (b), surface friction (c), bottom friction (d), advection (e), and local acceleration (f) for water column in winter according to Eq. (5) (units:  $10^{-4} \text{ m}^2/\text{s}^2$ ).

The two blue arrows indicate the two TWC branches. The two triangles indicate the two regions with significant fluctuation north of Taiwan (P1) and in the inshore area (P2).

950

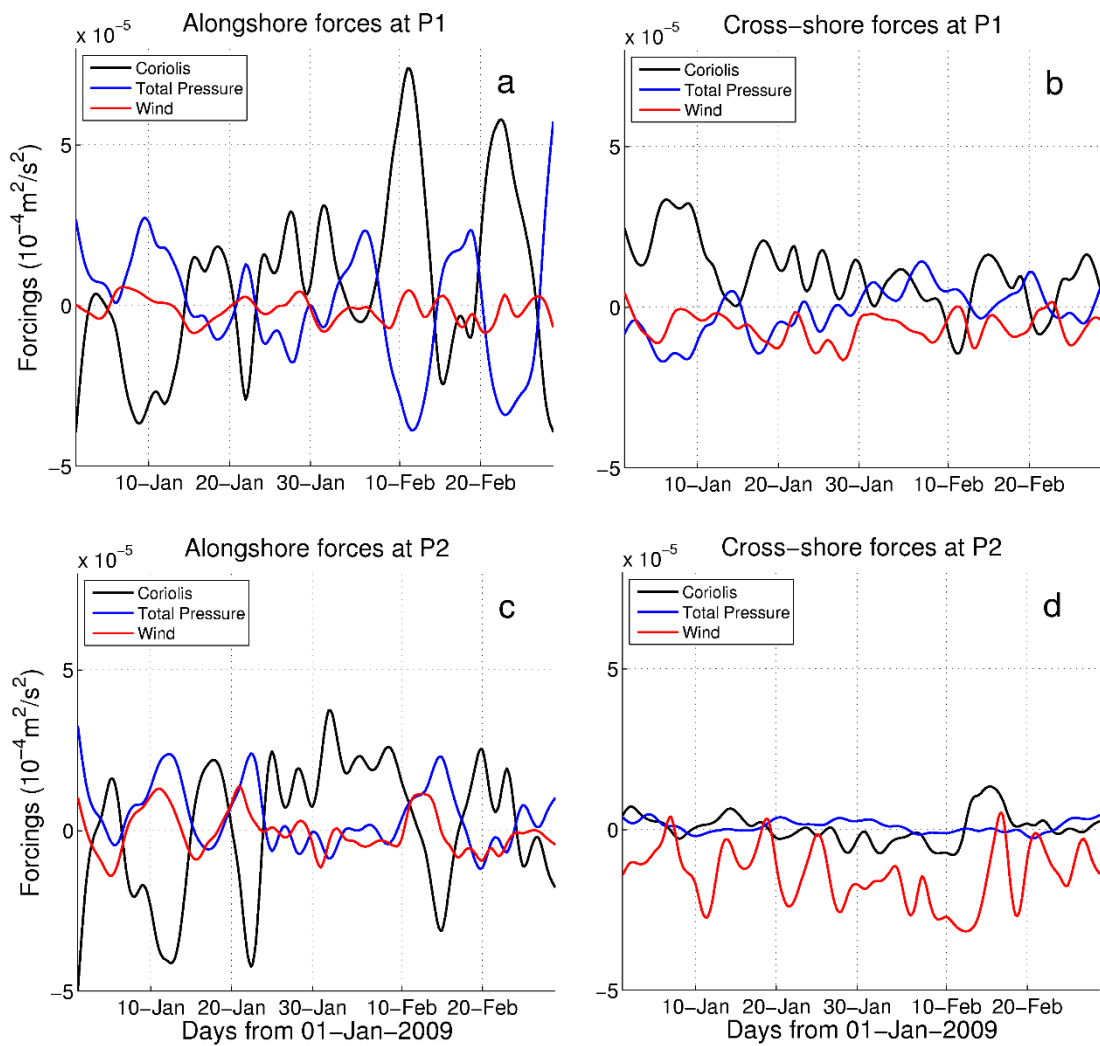


Figure 13: Variations in Coriolis force, total pressure, and wind in the alongshore direction at P1 (a), the cross-shore direction at P1 (b), the alongshore direction at P2 (c), and the cross-shore direction at P2 (d)

955 according to Eq. (5).



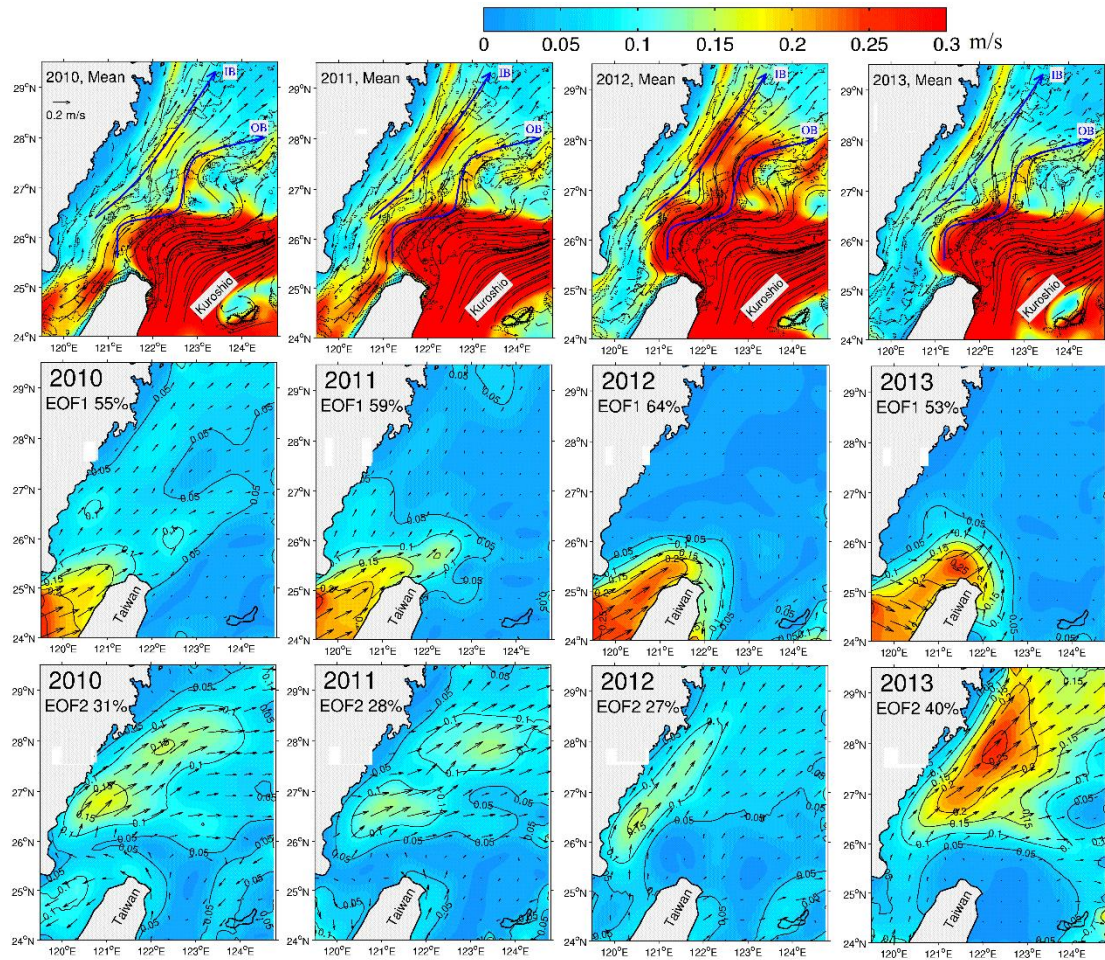


Figure 14: Mean currents (upper panels) and synoptic fluctuations (EOF1 in middle panels and EOF2 in bottom panels) in winters of 2010-2013. The black arrows show the velocity (m/s) in the layer of VMV and the color shows the current speed. The two blue arrows with label IB and OB represent the flow axes of the inshore branch and offshore branch, respectively.

960

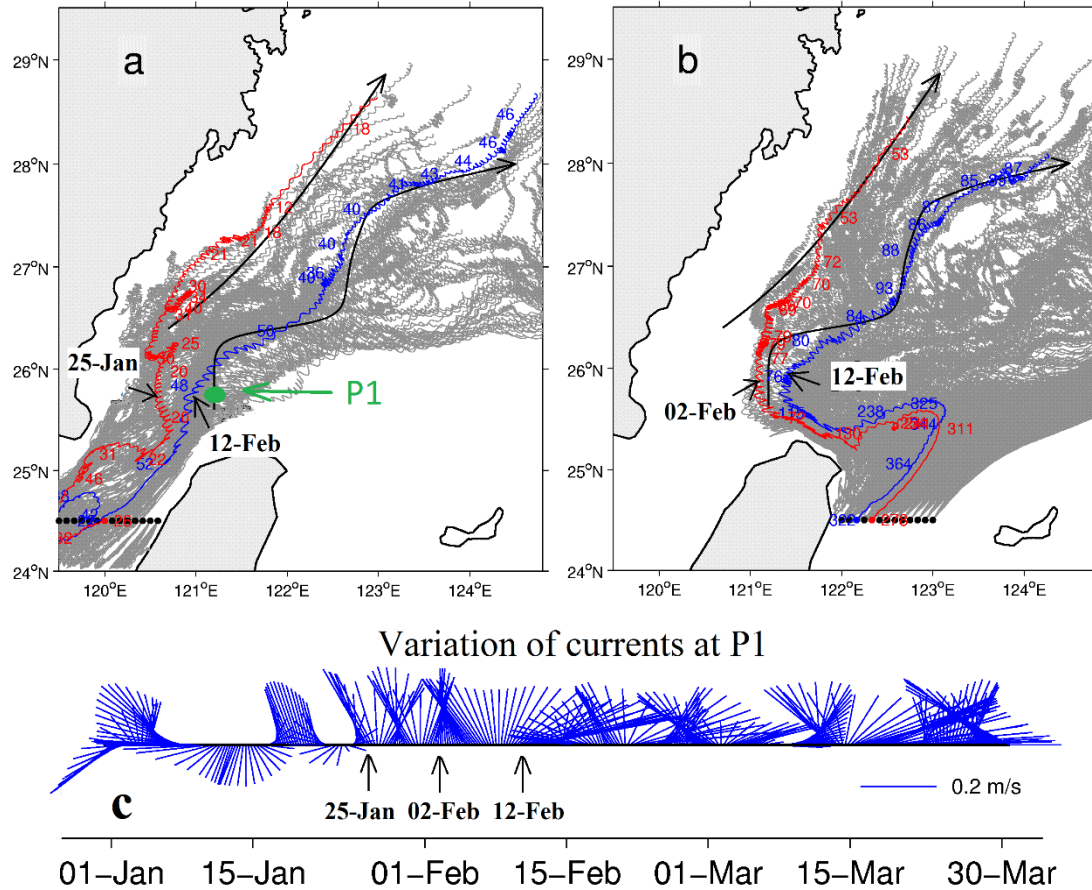


Figure 15: Traces of TSC water (a) and Kuroshio water (b) in winter, with the variation of surface currents at the original location of P1 (c). The black dots represent the release locations of tracers. The gray lines show the entire trajectories of the tracers. The red lines and blue lines are selected trajectories, which are close to the inshore branch and offshore branch, respectively. The dates show the times that selected tracers reached the origin location P1; note that the location of P1 is not fixed but varies with time. The numbers are the depths of the tracers, which are labeled at an interval of six days. The two black arrows represent the two TWC branches.

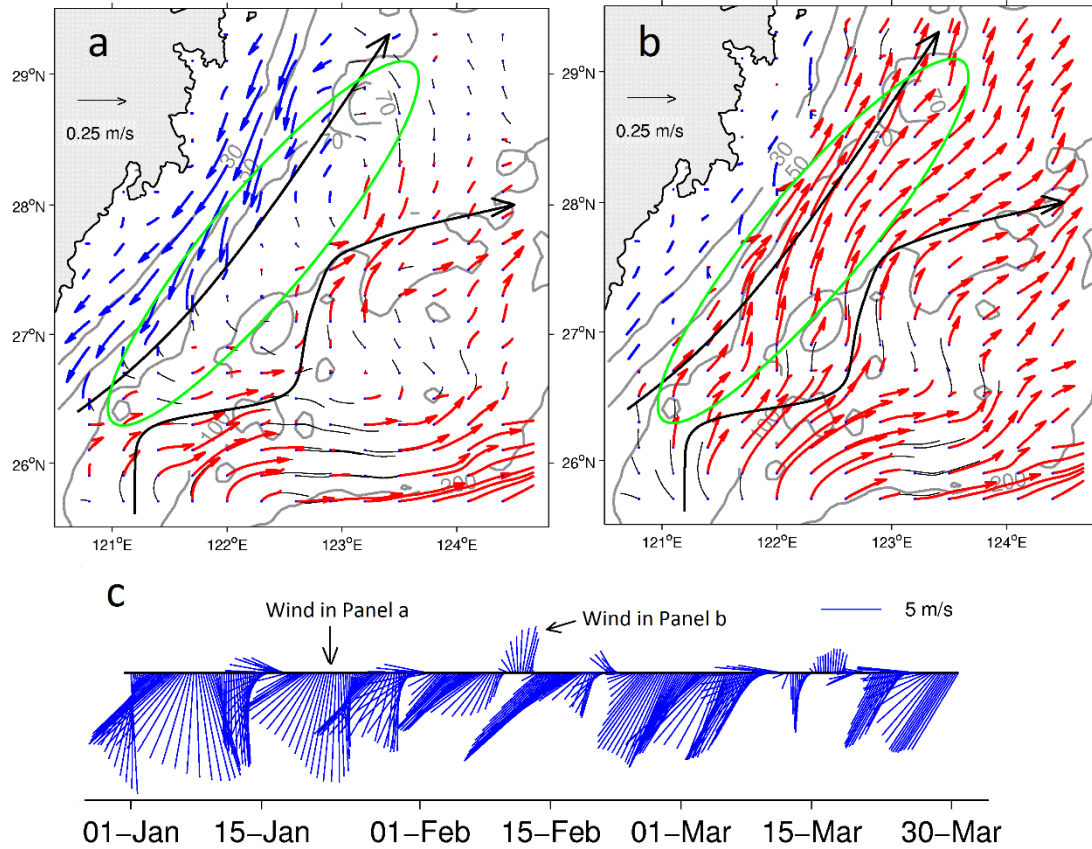


Figure 16: The VMV under the northerly wind (a) and southerly wind (b). Panel (c) shows the variation of wind in winter. Blue vectors and red vectors show the southwestward coastal current and the northeastward TWC, respectively. Gray contours indicate the 30, 50, 70, and 100 m isobaths. The two black arrows represent the two TWC branches. The green ellipse indicates the inshore area with significant fluctuation.